Bioactive Materials 33 (2024) 223–241

Contents lists available at ScienceDirect

Bioactive Materials

journal homepage: www.keaipublishing.com/en/journals/bioactive-materials

Simvastatin/hydrogel-loaded 3D-printed titanium alloy scaffolds suppress osteosarcoma via TF/NOX2-associated ferroptosis while repairing bone defects

Zehao Jing [a,b,c,1], Wanqiong Yuan [a,b,c,1], Jiedong Wang [a,b,c,1], Renhua Ni [a,b,c], Yu Qin [d], Zhinan Mao [d], Feng Wei [a,b,c], Chunli Song [a,b], Yufeng Zheng [d,***], Hong Cai [a,b,**], Zhongjun Liu [a,b,c,*]

[a] Department of Orthopedics, Peking University Third Hospital, Beijing, 100191, People's Republic of China
[b] Engineering Research Center of Bone and Joint Precision Medicine, Ministry of Education, Beijing, 100191, People's Republic of China
[c] Beijing Key Laboratory of Spinal Disease Research, Beijing, 100191, People's Republic of China
[d] School of Materials Science and Engineering, Peking University, Beijing, 100871, People's Republic of China

ARTICLE INFO

Keywords:
3D-printed titanium alloy
Implant
Simvastatin
Osteosarcoma
Ferroptosis

ABSTRACT

Postoperative anatomical reconstruction and prevention of local recurrence after tumor resection are two vital clinical challenges in osteosarcoma treatment. A three-dimensional (3D)-printed porous Ti6Al4V scaffold (3DTi) is an ideal material for reconstructing critical bone defects with numerous advantages over traditional implants, including a lower elasticity modulus, stronger bone-implant interlock, and larger drug-loading space. Simvastatin is a multitarget drug with anti-tumor and osteogenic potential; however, its efficiency is unsatisfactory when delivered systematically. Here, simvastatin was loaded into a 3DTi using a thermosensitive poly (lactic-co-glycolic) acid (PLGA)-polyethylene glycol (PEG)-PLGA hydrogel as a carrier to exert anti-osteosarcoma and osteogenic effects. Newly constructed simvastatin/hydrogel-loaded 3DTi (Sim-3DTi) was comprehensively appraised, and its newfound anti-osteosarcoma mechanism was explained. Specifically, in a bone defect model of rabbit condyles, Sim-3DTi exhibited enhanced osteogenesis, bone in-growth, and osseointegration compared with 3DTi alone, with greater bone morphogenetic protein 2 expression. In our nude mice model, simvastatin loading reduced tumor volume by 59%–77 % without organic damage, implying good anti-osteosarcoma activity and biosafety. Furthermore, Sim-3DTi induced ferroptosis by upregulating transferrin and nicotinamide adenine dinucleotide phosphate oxidase 2 levels in osteosarcoma both *in vivo* and *in vitro*. Sim-3DTi is a promising osteogenic bone substitute for osteosarcoma-related bone defects, with a ferroptosis-mediated anti-osteosarcoma effect.

1. Introduction

Osteosarcoma is a common primary malignant bone tumor that primarily affects children and adolescents [1]. Due to its highly invasive and metastatic nature, osteosarcoma significantly impacts the quality of life and overall survival of patients, with a five-year survival rate ranging from 60 to 80 % [2]. Achieving a radical cure relies on accurate tumor mass removal [3]. However, for limb salvage procedures and cases with indistinguishable tumor-margins, ideal tumor-free resection often fails [4,5]. Although perioperative neoadjuvant chemotherapy has improved survival rates, the limited drug concentrations in the tumor area and the severe systemic adverse effects of traditional chemotherapy drugs hinder its therapeutic efficacy [6,7]. Conventional bone

Peer review under responsibility of KeAi Communications Co., Ltd.
* Corresponding author. Department of Orthopedics, Peking University Third Hospital, Beijing, 100191, People's Republic of China.
** Corresponding author. Department of Orthopedics, Peking University Third Hospital, Beijing, 100191, People's Republic of China.
*** Corresponding author.
E-mail addresses: 1789081128@qq.com (Z. Jing), yuanwanqiong@bjmu.edu.cn (W. Yuan), xhwangjd@163.com (J. Wang), tiffanyni@126.com (R. Ni), qinyu95@126.com (Y. Qin), znmao@pku.edu.cn (Z. Mao), weifeng@bjmu.edu.cn (F. Wei), schl@bjmu.edu.cn (C. Song), yfzheng@pku.edu.cn (Y. Zheng), hongcai@bjmu.edu.cn (H. Cai), zjliu@bjmu.edu.cn (Z. Liu).
[1] Zehao Jing, Wanqiong Yuan and Jiedong Wang contributed equally to this study.

https://doi.org/10.1016/j.bioactmat.2023.11.001
Received 17 August 2023; Received in revised form 18 October 2023; Accepted 2 November 2023

List of abbreviations

3DTi	Three-dimensional (3D)-printed porous Ti6Al4V scaffold
PGLA	poly(lactic-co-glycolic) acid
PEG	polyethylene glycol
Sim-3DTi	simvastatin/hydrogel-loaded 3DTi
BMP-2	bone morphogenetic protein 2
TF	transferrin
NADPH	nicotinamide adenine dinucleotide phosphate
NOX2	NADPH oxidase 2
VEGF	vascular endothelial growth factor
NOXs	NADPH oxidases
ROS	reactive oxygen species
EBM	electron beam melting
STL	standard triangulation language
SEM	scanning electron microscopy
FE-SEM	field emission SEM
PBS	phosphate-buffered saline
DMEM	Dulbecco's Modified Eagle Medium
FBS	fetal bovine serum
CCK-8	Cell Counting Kit-8
AM	acetoxymethyl ester
PI	propidium iodide
H&E	hematoxylin and eosin
micro-CT	micro-computed tomography
ROI	region of interest
BV/TV	bone volume/tissue volume
TbSp	trabecular separation
rRT-PCR	Real-time reverse transcriptase-polymerase chain reaction
SDS	sodium dodecyl sulfate
DAB	diaminobenzidine
IOD	integrated optical density
IHC	immunohistochemistry
siRNA	silencing RNA
GSH	glutathione
MDA	malondialdehyde
SD	standard deviation
DEP	differently expressed protein
KEGG	Kyoto Encyclopedia of Genes and Genomes
GO	Gene Ontology
rhBMP-2	recombinant human BMP-2
(SDF-1)α	stromal cell-derived factor 1

substitutes like titanium mesh have disadvantages, including poor shape matching, high elastic modulus, and a high incidence of bone resorption and endplate collapse when used for repairing critical bone defects. Consequently, development of novel functionalized scaffolds capable of repairing critical bone defects and preventing tumor recurrence is urgently needed [8].

Biomaterials have good biocompatibility and bioactive properties for stimulation of bone regeneration. It is a promising treatment option that the integrated biomaterials with the ability of bone regeneration combine tumor therapy [9,10]. Currently, 3D-printed titanium alloy (3DTi) is considered a superior bone substitute due to its numerous advantages over traditional implants, including a customized shape, a porous structure that enhances bone-implant interlock, and an adjustable lower elastic modulus that helps prevent stress shielding [11,12]. Previous studies have demonstrated that 3DTi can provide both immediate and long-term stability at the bone defect site through fusion at the bone-implant interface, eliminating the need for a bone graft [13,14]. However, the bioinert characteristic of 3DTi limits its ability to promote osteogenesis. This limitation can be overcome by incorporating growth factors, such as bone morphogenetic protein 2 (BMP-2) and vascular endothelial growth factor (VEGF), into the porous structure of 3DTi [15,16]. Furthermore, it has been shown that loading cisplatin into 3DTi can reduce the tumor burden surrounding the implant [17]. Therefore, it is feasible to utilize 3DTi for local drug administration to achieve both anti-osteosarcoma and osteogenic effects.

Simvastatin is a commonly used lipid regulator that has recently been found to play key roles in osteogenesis [18,19], and antibacterial effects [20,21]. Meanwhile, in comparison to most growth factors that enhance osteogenesis, simvastatin has a lower price, longer half-life, and better safety profile [19]. Previous studies have indicated the therapeutic potential of simvastatin for treating osteosarcomas, either alone or in combination with chemotherapy agents [22,23]. Therefore, simvastatin is an ideal drug for treating osteosarcoma-related bone defects. However, simvastatin undergoes significant first-pass metabolism, meaning systemic administration results in low intra-osseous and intratumoral drug concentrations and unsatisfactory osteogenic and antineoplastic efficacy [19,24,25]. To avoid simvastatin distribution to non-target sites, topical drug delivery to the osteosarcoma-related bone defects using 3DTi was proposed in this study.

Poly (lactic-co-glycolic) acid (PLGA)-polyethylene glycol (PEG)-PLGA hydrogel is a commonly employed drug carrier with degradation products that have received approval from the US Food and Drug Administration (FDA), rendering it suitable for clinical use [26,27]. It is also a reversible thermosensitive gelation, which makes convenient handling and ease of application [28]. Nevertheless, its mechanical strength is inadequate for serving as a bone substitute. Therefore, the injection of a drug-loaded PLGA-PEG-PLGA hydrogel into the porous structure of 3DTi not only addresses the mechanical limitations of hydrogels but also enables localized drug application.

Although numerous studies have demonstrated the anti-tumor effects of simvastatin, the precise underlying mechanisms remain unclear [29,30]. Through proteomic sequencing analysis, this study identified the involvement of ferroptosis-related proteins, specifically transferrin (TF) and nicotinamide adenine dinucleotide phosphate (NADPH) oxidase 2 (NOX2), in the suppression of osteosarcoma by simvastatin. Ferroptosis is a form of programmed cell death characterized by iron-mediated oxidative damage, distinct from apoptosis [31]. It is initiated through two main pathways: the intrinsic pathway, which involves iron transporter TF activation to induce iron overload, and the extrinsic pathway, which involves NADPH oxidases (NOXs) triggering reactive oxygen species (ROS) production for lipid peroxidation [32]. Tumor cells are particularly susceptible to ferroptosis, potentially due to the activation of tumor suppressors during ferroptosis initiation and the inherently high ROS levels present in tumor cells [33]. Therefore, targeting ferroptosis in osteosarcoma cells represents a viable strategy for anti-neoplastic treatment.

In this study, we developed a simvastatin/hydrogel-loaded 3DTi (Sim-3DTi) and evaluated its effects on osteogenesis and osteosarcoma in a rabbit condyle bone defect model and an osteosarcoma-bearing nude mouse model. Additionally, we conducted next-generation proteome sequencing to identify the pathways associated with the anti-osteosarcoma mechanism of localized simvastatin. These findings were further validated through *in vitro* and *in vivo* experiments. This study is significant as it represents the first preclinical investigation to achieve both anti-tumor and osteogenic functionality in 3DTi through the loading of a single drug. Furthermore, our research establishes that simvastatin activates TF and NOX2, resulting in the ferroptosis of osteosarcoma. These findings contribute to our understanding of the mechanism by which simvastatin acts against osteosarcoma and hold great potential for future clinical applications.

2. Materials and methods

2.1. Fabrication of 3DTi

We fabricated the 3DTi (Ø5 mm × L6 mm, pore size of 640 μm, and strut diameter of 400 μm) using an electron beam melting (EBM) S12 system (Arcam AB, Gothenburg, Sweden), as previously described [16,17]. Typically, a predesigned cylindrical 3D model is converted into a standard triangulation language (STL) file and transferred to the EBM machine. The medical-grade titanium alloy Ti6Al4V powder (particle size: 45–100 μm) was melted layer by layer according to the STL data and solidified by cooling afterward. The prepared scaffolds were ultrasonically cleaned successively in acetone, ethyl alcohol, and deionized water for 15 min each. The physical parameters of 3DTi, including true density, specific surface area, porosity, and nominal stress were measured by helium gas pycnometer, Kr-BET method, mercury porosimeter, and mechanical testing system respectively as previously described [17].

2.2. Preparation of simvastatin/hydrogel-loaded 3DTi (Sim-3DTi)

The hydrogel was prepared as previously described [34,35]. Briefly, the PLGA (1500–2000)-PEG (1000–1500)-PLGA (1500–2000) thermosensitive hydrogel (Shanghai Yuanye Bio-Technology Co., Ltd., Shanghai, China) was suspended in deionized water with stirring at a mass ratio of 1:4. After incubation for seven nights at 4 °C, the hydrogel completely dissolved and formed a clear viscous solution. Simvastatin (National Institutes for Food and Drug Control, Beijing, China) at final concentrations of 0.5, 1, 1.25, 2.5, 5, 10, 15, and 20 mg/mL was loaded into the hydrogel. The 3DTi were placed inside a custom-made chamber and filled with the loaded hydrogel at 4 °C. The samples were warmed to room temperature (18–25 °C) before implantation to form the Sim-3DTi (Fig. 1A) and named Sim 0.5, Sim 1, Sim 1.25, Sim 2.5, Sim 5, Sim 10, Sim 15, and Sim 20, according to the final concentration of simvastatin.

2.3. Characterization of the Sim-3DTi

Sim-3DTi, 3DTi, hydrogel, and released simvastatin were observed using cryogenic scanning electron microscopy (SEM). Briefly, the samples were placed in the slots of a stub, plunged into a liquid-nitrogen slush, and transferred to a cryo-preparation chamber (PP3010T; Cryo-SEM Preparation System, Quorum Technologies, Newhaven, UK). After freeze-fracture-treatment, sublimation at −90 °C for 5 min, and sputtering with platinum at 10 mA for 60 s, the samples were examined using field emission SEM (FE-SEM, JSM7900F, JEOL, Tokyo, Japan) at 3.0 kV accelerating voltage. Thereafter, the elemental distribution and chemical composition of the samples were characterized using energy-dispersive spectroscopy (EDS, Aztec X-Max50, Oxford, UK).

The rheological property of PLGA-PEG-PLGA thermosensitive hydrogel was performed in dynamic oscillation mode on a rheometer (Physica MCR 302, Paar Physica, Germany) at a fixed frequency of 1 Hz and 0.1 % stress amplitude. All measurements were performed at temperatures ranging from 0 to 50 °C and at a heating rate of 1 °C/min. The elastic modulus (G') and the viscous modulus (G'') were determined tested by rotational rheometer (RheolabQC, Anton Paar, USA).

The hydrogel degradation process of Sim-3DTi was characterized as previously reported [17]. Briefly, 6 Sim-3DTis at each concentration were placed in a glass bottle and immersed in 250 mL of phosphate-buffered saline (PBS, pH 5.5) at 37 °C to imitate the post-surgical acidic conditions and extracellular microenvironment of tumor cells. Of note, three of the Sim-3DTis at each concentration were stained in green with calcein to improve visualization and photographed using a stereo microscope (M205 FA, Leica, Germany) with a 490-nm excitation filter every 3 days. The fluorescence intensity of Sim-3DTis at each time point were calculated using Image-Pro Plus 6.0 software. The other three Sim-3DTis at each concentration were weighed accurately at the same time. The mass remaining of hydrogel is equal to the mass of Sim-3DTi at each time point minus that of 3DTi.

The releasing curve of simvastatin was determined as previously described [17]. Briefly, Sim-3DTi at concentration of 2.5 mg/mL and 5 mg/mL were immersed in 2 mL of PBS (PH 5.5) in two tubes, respectively. At determined time point, 1 mL of extracting solution was collected from each tube and equal volume of PBS was supplemented into tubes. The concentration of released simvastatin in each extracting solution was measured using an inductively coupled plasma mass spectrometer (ICP-MS, Xseries II; Thermo Fischer Scientific, Waltham, MA, USA), and then calculated to acquire the releasing curve.

2.4. In vitro anti-osteosarcoma effect and bio-safety of Sim-3DTi

2.4.1. Cell proliferation

The viability of human osteosarcoma cells (143B) and mouse fibroblasts (L929) (American Type Culture Collection [ATCC], USA) co-cultured with 3DTi and Sim-3DTi was quantified as described previously [17]. Briefly, the cells were seeded into 48-well plates (15,000 cells per well in 600 mL of Dulbecco's Modified Eagle Medium [DMEM] containing 10 % fetal bovine serum (FBS) and 1 % penicillin/streptomycin), and incubated at 37 °C under a 5 % CO_2 atmosphere for 24 h. Then, 3DTi (control group) or Sim-3DTis at different concentrations (Sim 0.5, Sim 1, Sim 1.25, Sim 2.5, Sim 5, Sim 10, Sim 15, and Sim 20) were added to separate wells. The culture medium was replaced with DMEM daily. After incubation for one, three, and five days, cell viability was calculated using the Cell Counting Kit-8 (CCK-8, Dojindo, Japan) according to the manufacturer's instructions, and the optical densities were measured using a microplate reader (Varioskan Flash; Thermo Fisher Scientific, Cleveland, OH, USA) at a 450 nm wavelength.

2.4.2. Cell migration

Cell migration was assessed using Transwell chambers (8-μm pore size, BD Biosciences, NJ, USA). After three days of incubation with 3DTi (control group) or Sim-3DTi, 143B cells were cultured overnight in a serum-free medium before initiating the experiments. The following day, 3×10^4 cells in 0.25 mL serum-free medium were seeded into the upper chamber, and medium (0.5 mL) with 10 % FBS was added to the lower chamber. After incubation at 37 °C for 12 h, the chambers were disassembled, and the membranes were fixed in 4 % paraformaldehyde for 10 min and stained with 2 % crystal violet for 10 min. The number of cells was counted, and images were obtained under a microscope (100 × magnification).

2.4.3. Cell survival

Calcein-acetoxymethyl ester (AM)/propidium iodide (PI) double staining kit (Solarbio, Beijing, China) was used to measure cell survival in 143B and L929 cells co-cultured with 3DTi and Sim-3DTi. Briefly, the cells were seeded into 48-well plates (15,000 cells per well in 600 mL of DMEM containing 10 % FBS and 1 % penicillin/streptomycin), and incubated at 37 °C under a 5 % CO_2 atmosphere for 24 h. Then, 3DTi (control group) or Sim-3DTi was added to the wells. The culture medium was replaced with DMEM daily. After three days of incubation, cells were incubated with calcein AM (2 μM) and PI (4.5 μM) at 37 °C for 15 min. Then, the live and dead cells were observed using 490- and 545-nm excitation filters, respectively, under a confocal laser scanning microscope (TCS SP8, Leica, Germany). The percentage of cell survival rate was calculated based on the fluorescence intensity using Image-Pro Plus 6.0 software.

2.5. In vivo anti-osteosarcoma effect and bio-safety of Sim-3DTi

2.5.1. Tumor-bearing nude mice model and grouping

All animal experimental protocols were approved by the Peking University Institutional Review Board on Biomedical Ethics in the Care

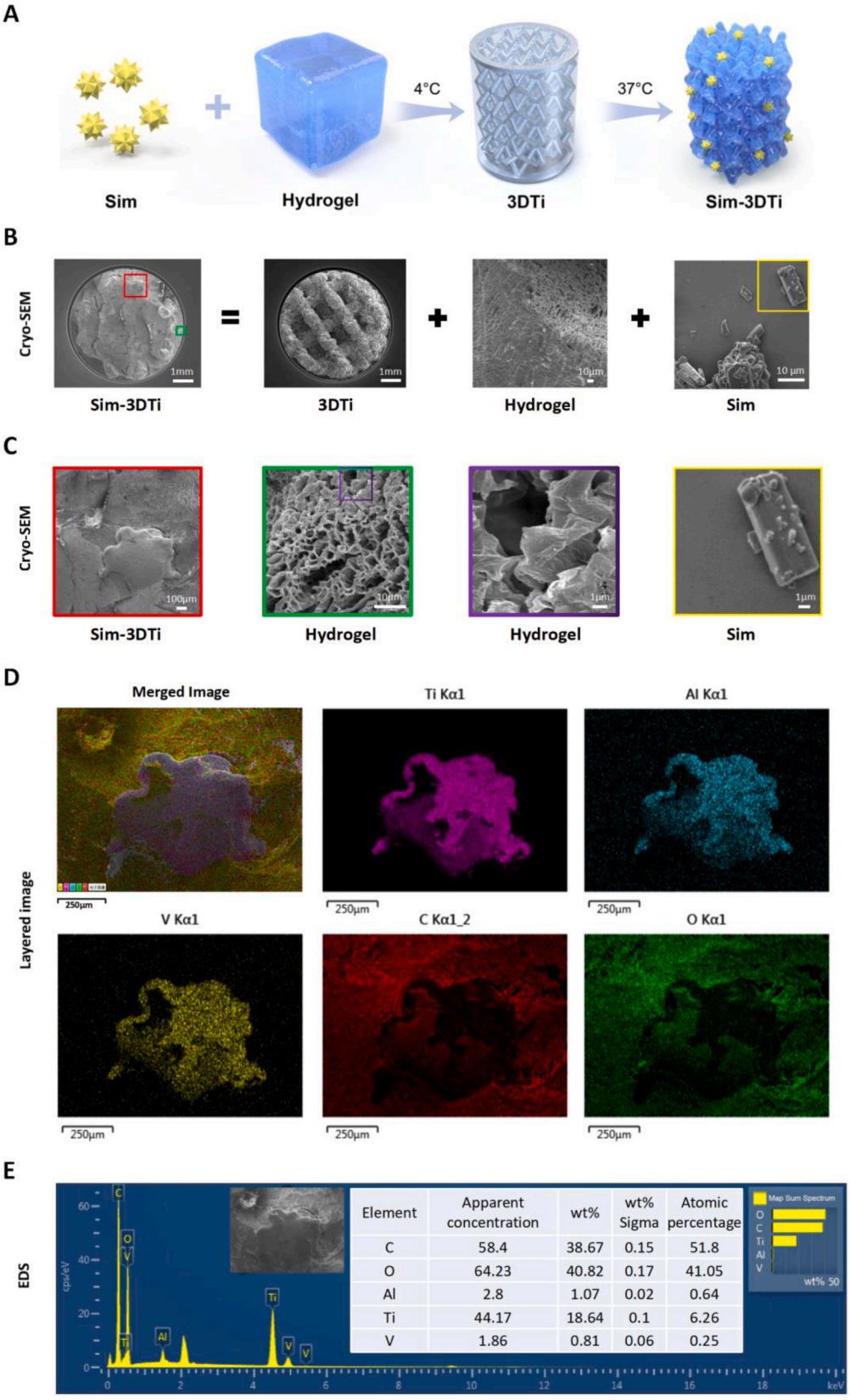

Element	Apparent concentration	wt%	wt% Sigma	Atomic percentage
C	58.4	38.67	0.15	51.8
O	64.23	40.82	0.17	41.05
Al	2.8	1.07	0.02	0.64
Ti	44.17	18.64	0.1	6.26
V	1.86	0.81	0.06	0.25

Fig. 1. Characterization of Sim-3DTi using scanning electron microscopy (SEM) and energy-dispersive spectroscopy (EDS). (A) Schematic diagram of Sim-3DTi construction protocol. (B–C) Representative SEM images of Sim-3DTi, 3DTi, PLGA-PEG-PLGA hydrogel and simvastatin particles. 3DTi has a macroporous diamond lattice structure. Hydrogel displays a microporous structure. Rod-like simvastatin, about 5–10 μm in length. (D–E) Representative EDS layered images and quantitative elemental analysis of Sim-3DTi. The surface of Sim-3DTi was dominated by carbon and oxygen elements, rather than titanium, aluminum, and vanadium, indicating that the hydrogel PLGA-PEG-PLGA wrapped the Ti6Al4V scaffold.

and Use of Laboratory Animals (Project Number: LA2020465). Briefly, six-week-old female BALB/c nude mice (Charles River, Beijing, China) weighing 13–17 g were used to construct a tumor-bearing nude mouse model. Osteosarcoma 143B cells (2.0×10^6) were subcutaneously injected into the right scapula of mice. The model was considered successfully established when the tumor volume reached approximately 100 mm^3 over 10 days [17].

Mice with similar body weights and tumor sizes were randomly divided into three groups (n = 6). A scaffold was placed subcutaneously adjacent to the tumor in each mouse. Among them, mice implanted with 3DTi were defined as the control group, while mice implanted with Sim-3DTi loaded with 2.5 mg/mL and 5 mg/mL simvastatin were defined as the Sim 2.5 and Sim 5 groups, respectively.

2.5.2. Tumor volume and body weight

The tumor volume and body weight were measured twice per week for up to 18 days. The following equation was used to calculate the tumor volume:

$V = L \times W^2 \times 0.5$, where L (mm) and W (mm) are the largest and smallest tumor mass diameters, respectively [36].

2.5.3. Hematoxylin and eosin (H&E) staining

After sacrifice, the tumors, hearts, livers, spleens, lungs, and kidneys of the mice were collected and fixed in 4 % w/v paraformaldehyde for histological analysis. The tissues were embedded in paraffin and sectioned into 5 μm-thick slices. The slices were then stained with H&E to evaluate tumor pathology and organ damage.

2.6. Osteogenic effect in vivo

2.6.1. Rabbit bone defect model and grouping

Twenty-five-week-old female New Zealand white rabbits (weighing 3.5 ± 0.3 kg, Charles River, Beijing, China) were equally divided into three groups (n = 5). To construct the bone defect model, the rabbits were anesthetized with pentobarbital sodium (30 mg/kg, i. p.) [37], cylindrical defects with a 5-mm diameter and 6-mm depth were created in the lateral femoral condyles, and 3DTi were implanted. Rabbits implanted with 3DTi were defined as the control group, whereas rabbits implanted with Sim-3DTi loaded with 2.5 mg/mL and 5 mg/mL simvastatin were defined as the Sim 2.5 and Sim 5 groups, respectively.

2.6.2. Sampling

Five rabbits from each group were euthanized four weeks post implantation. Femur specimens (10 from each group) of sacrificed rabbits were collected for micro-computed tomography (micro-CT) imaging, undecalcified histological slicing, and BMP-2 detection.

2.6.3. Micro-CT analysis

All femur specimens from each group were scanned using micro-CT (Siemens, Erlangen, Germany) at a scanning rate of 6°/min and a resolution of 9 μm. The X-ray source voltage was 80 kV, and the beam current was 80 mA using filtered bremsstrahlung radiation. A 1-mm aluminum filter was used during scanning. The micro-CT images were then reconstructed using multimodal 3D visualization software (Inveon Research Workplace; Siemens, Germany). Bone was distinguished from soft tissues and titanium alloy scaffolds by the partitioning of different Hounsfield units (HUs). Bone was defined in the range of 1000–2250 HU. After reconstruction, the peripheral 500-μm region around and the intra-porous space within the scaffolds were selected as the region of interest (ROI). In the ROI, the bone volume/tissue volume (BV/TV, the ratio of bone volume to total volume) and trabecular separation (Tb.Sp, mean width of the medullary cavity between bone trabeculae) were calculated using Inveon Research Workplace software (Siemens, Germany) [17].

2.6.4. Undecalcified bone histology

Undecalcified bone sections were prepared for bone in-growth and osseointegration analyses, as previously described [38]. Briefly, specimens were fixed in 10 % formalin for 14 days and dehydrated in serial ethanol concentrations (40 %, 75 %, 90 %, 95 %, and 100 %) for three days. The specimens were embedded in methyl methacrylate and sectioned using a power saw with a diamond blade from the EXAKT system (EXAKT Apparatebau, Hamburg, Germany). Ground sections of 40–50 μm were then prepared using this system and subjected to Masson–Goldner trichrome staining (the bone tissues and osteoid tissues were stained green and red/orange, respectively; the scaffolds appeared black). The stained sections were photographed using a NanoZoomer digital slide scanner (Hamamatsu Photonics, Hamamatsu, Japan). Quantitative analysis was performed using Image-Pro Plus software (version 6.0), with a middle longitudinal section of each block used to determine both bone in-growth and osseointegration. Ten slices were analyzed for each group. The bone in-growth value was defined as the percentage of new bone within the pores and was equal to the area of the bone over the pore area. The osseointegration was measured as the fraction of the scaffold surface area in contact with the bone. The tissue sections were viewed at high magnification to accurately calculate the circumference and length of the bone-covered scaffold. The osseointegration value corresponds to the length of the scaffold covered by the bone divided by the scaffold circumference.

2.6.5. Real-time reverse transcriptase-polymerase chain reaction (rRT-PCR)

Immediately after sacrifice, a small piece of new bone around the Sim-3DTi was collected from each sample rabbit for rRT-PCR, performed as previously described [39,40]. Briefly, total RNA was extracted from cells or tissues using Trizol reagent (Life Technologies, USA) and cDNA was generated using a First-Strand cDNA Synthesis Kit (Tiangen, Beijing, China) according to standard protocols. Amplifications were performed using the SYBR Green PCR Master Mix Kit (Biosystems, USA) according to the manufacturer's instructions. BMP-2 expression was calculated using the $2-\Delta\Delta Ct$ method. GAPDH expression was used as control. All reactions were repeated in triplicate. Primers: BMP-2-F: 5′-AGCTTTGGGAGACGACAGC-3'; R: 5′-GGCTCGTGTTCTGATTCACC-3'; GAPDH-F: 5′-TTGTCGCCATCAATGATCCAT-3'; GAPDH-R: 5′-GATGACCAGCTTCCCGTTCTC-3'. F: Forward primer; R: Reverse prime.

2.7. Mechanism of the anti-osteosarcoma effect of local simvastatin delivery

2.7.1. Next-generation proteome sequencing

As reported previously [39], the tumors of mice in the control and Sim 5 groups were collected immediately after sacrifice, frozen in liquid nitrogen, ground, and lysed in sodium dodecyl sulfate (SDS) lysis Buffer (Beyotime, Haimen, China) containing a protease inhibitor (Thermo Fisher Scientific) under sonication. After centrifugation, the supernatant was collected and the protein concentration was determined using the Bradford assay. Proteins extracted from the tumor tissues were alkylated and enzymatically digested. Peptides were labeled with iTRAQ reagents (AB SCIEX, Foster City, CA, USA) and separated using an offline high pH (7.5, or 10) reversed-phase column (Agilent, Santa Clara, CA, USA). All mass spectrometry data were analyzed using the MaxQuant software (version 1.6.17.0).

2.7.2. Immunohistochemistry

Briefly, tumor tissue specimens were cut into 10-μm sections after dewaxing and hydration. The soaked sections were blocked with 0.3 % hydrogen peroxide at 25 ± 2 °C for 10 min, then incubated with normal goat serum for 10 min and incubated overnight at 4 °C with the following primary antibodies: anti-Ki67 antibody (Abcam, Cambridge, UK, dilution: 1:200), anti-transferrin (Abcam, Cambridge, UK, dilution: 1:200) and anti-NOX2 (Abcam, UK, dilution: 1:200). The next day, the

sections were washed with PBS and incubated with biotinylated secondary antibodies at 37 °C for 45 min. The sections were washed again with PBS and incubated with horseradish peroxidase-labeled streptavidin at 37 °C. The samples were developed using diaminobenzidine (DAB) and stained with hematoxylin. After washing, dehydration, lucidification, and mounting, all sections were photographed using a NanoZoomer digital slide scanner (Hamamatsu Photonics). The integrated optical density (IOD) was measured to accurately reflect total protein expression. Positive immunohistochemistry (IHC) areas were analyzed using Image-Pro Plus 6.0 [17].

2.7.3. Cell lines and culture

The 143B osteosarcoma cells and L929 cells were cultured in DMEM (HyClone, Logan, UT, USA) supplemented with 10 % fetal bovine serum (Gibco, Grand Island, NY, USA) and 1 % penicillin/streptomycin solution (Gibco, USA) at 37 °C in a 5 % CO_2 atmosphere.

2.7.4. Silencing RNA (siRNA)-mediated gene knockdown [40]

All siRNAs were purchased from Beijing Yibaike Co. Ltd., Beijing, China. To knock down TF and NOX2, the siRNA sequences were chosen as follows:

si-hTransferrin-1:5′-GUGUCUGGCUGUCCCUGAUAATT-3′,
si-hTransferrin-2:5′-CUUGAUCUGGGAGCUUCUCAATT-3′,
si-hNOX2-1:5′-GCUGUGCCUCAUAUUAAUUTT-3′,
si-hNOX2-2:5′- CCAUGGAGCUGAACGAAUUTT-3′.
The negative control was 5′-UUCUCCGAACGUGUCACGUdTdT3′.

Briefly, 143B cells were seeded in six-well plates at a density of 2×10^5 cells per well and transfected with siRNA using Lipofectamine-3000 reagent (Invitrogen, Carlsbad, CA, USA) according to the manufacturer's protocol. The cells were then incubated for two days, and the knockdown efficacy was validated using Western blot.

2.7.5. Western blot assay

Western blot analysis was performed as previously described [40]. The primary antibodies including anti-β-actin (Abcam, UK), anti-TF (Abcam, UK), and anti-NOX2 (Abcam, UK) were purchased commercially. Protein bands were photographed using an ImageQuant LAS500 imager (GE, Marlborough, MA, USA).

2.7.6. Transmission electron microscopy

Osteosarcoma 143B cells were collected and fixed with 2.5 % glutaraldehyde fixed solution (ASPEN Biotechnology, Wuhan, China) for 4 h at 4 °C. After rinsing with PBS, the samples were fixed with 1 % osmium for 2 h at 25 ± 2 °C and dehydrated using a gradient of ethanol. Next, the samples were infiltrated with acetone and embedded in SPI-PON 812 (SPI Supplies, West Chester, PA, USA). Finally, the samples were sectioned into 60 nm-thick slices and photographed using a transmission electron microscope (Tecnai G2 F20 S-TWIN, FEI, Eindhoven, the Netherlands).

2.7.7. Measurement of ferrous irons in mitochondria

Briefly, 143B cells were seeded in confocal dishes and subjected to different treatments at 37 °C in a 5 % CO_2 incubator. A total of 200 μL working solution containing 5 μmol/L Mito-FerroGreen and 200 nmol/L MitoBright Deep Red (Dojindo Molecular Technologies, Tokyo, Japan) were added to the cells which were then incubated for a further 30 min. The supernatant was discarded, and the cells were washed with Hanks' Balanced Salt Solution. Then, 100 mol/L ammonium iron (II) sulfate was added to the cells, which were then incubated under the same conditions for 1 h. The cells were photographed using a confocal laser scanning microscope (TCS SP8, Leica, Germany).

2.7.8. Measurement of glutathione (GSH) and malondialdehyde (MDA)

Intracellular GSH was measured using a GSH kit (Nanjing Jiancheng Bioengineering Institute, Nanjing, China) according to the manufacturer's protocol. The GSH content was calculated according to the absorbance at 405 nm and standardized using the protein concentration. Intracellular MDA was measured using an MDA kit (Nanjing Jiancheng Bioengineering Institute, Nanjing, China) according to the manufacturer's protocol. The MDA content was calculated according to the absorbance at 530 nm and standardized using the protein concentration.

2.8. Statistical analysis

Data are presented as mean ± standard deviation (SD). Statistical analyses were performed using SPSS software (version 12.0). A one-way analysis of variance (ANOVA) test followed by Tukey's post-hoc test was applied to data from experiments involving more than two groups, and a two-way *t*-test was used to analyze data from experiments with two groups at each time point. Statistical significance was set at $p < 0.05$.

3. Results

3.1. Sim-3DTi is a simvastatin/hydrogel-loaded Ti6Al4V scaffold that releases simvastatin for over 18 days

The physical parameters of 3DTi in this study were consistent with our previous results [17], proving that 3DTi's mechanical property is qualified as a bone substitute (Table S1). As shown in Fig. 1A, Sim-3DTi was constructed by injecting simvastatin-loaded hydrogel into 3DTi. To prevent hydrogel melting and collapse in the SEM vacuum, the Sim-3DTi samples were freeze-dried before being photographed using Cryo-SEM [41]. In the Cryo-SEM images, Sim-3DTi is a solid cylinder, composed of 3DTi with a macroporous diamond lattice structure, hydrogel with microporous structure and simvastatin particles with a rod-like appearance about 5–10 μm in length (Fig. 1B). The macropores of 3DTi can accommodate hydrogel, and the micropores of the hydrogel can accommodate simvastatin particles, thus making Sim-3DTi a stable complex (Fig. 1C). The EDS analysis revealed elemental enrichment of carbon and oxygen on the Sim-3DTi surface (Fig. 1D and E), distinct from those of titanium, aluminum, and vanadium, further verifying the element composition of 3DTi (Ti6Al4V) and hydrogel (PLGA--PEG-PLGA) and their close combination in Sim-3DTi. These results are consistent with those for a previously reported cisplatin/hydrogel-loaded 3DTi [17].

The rheological characteristic of PLGA-PEG-PLGA hydrogel was detected in this study. As shown in Fig. 2A, the hydrogel morphology was liquid at temperature of 4 °C, while gel at temperature of 37 °C (Fig. 2B). To quantitatively evaluate the gel formation with temperature variation, dynamic viscoelasticity measurements was performed using rheometer (Fig. 2C). With the increase of temperature, the hydrogel transformed from sol ($G' < G''$) to gel ($G' > G''$), and the transition temperature point was 19.053 °C.

A previous study [17] has shown that the release of encapsulated drugs in PLGA-PEG-PLGA is dependent on hydrogel degradation, so it is important to evaluate the hydrogel degradation rate in Sim-3DTi. In this research, the hydrogel degradation rate in Sim-3DTi was measured using direct observation (Fig. 2D), fluorescence intensity measurement (Fig. 2E) and mass weighing (Fig. 2F). Calcein was used to improve the hydrogel visibility. Fig. 2D shows that in a solution mimicking the extracellular acidic microenvironment of tumor cells, the Sim-3DTi hydrogel remained in the 3DTi pores for over 18 days, regardless of simvastatin concentration. With the degradation of hydrogel, the fluorescence intensity of Sim-3DTi and the mass remaining of hydrogel also decreased gradually. Overall, the simvastatin concentration (1–20 mg/mL) in the hydrogel did not significantly affect hydrogel degradation. And then, the releasing profiles of simvastatin were determined. As shown in Fig. 2H, simvastatin-2.5 mg and 5 mg continually released from 3DTis within 18 days, which was generally consistent with degradation profiles of hydrogels. This result confirmed that simvastatin was continuously released from the hydrogel pores as the hydrogel degraded rather than directly dissolving out. Therefore, the proposed

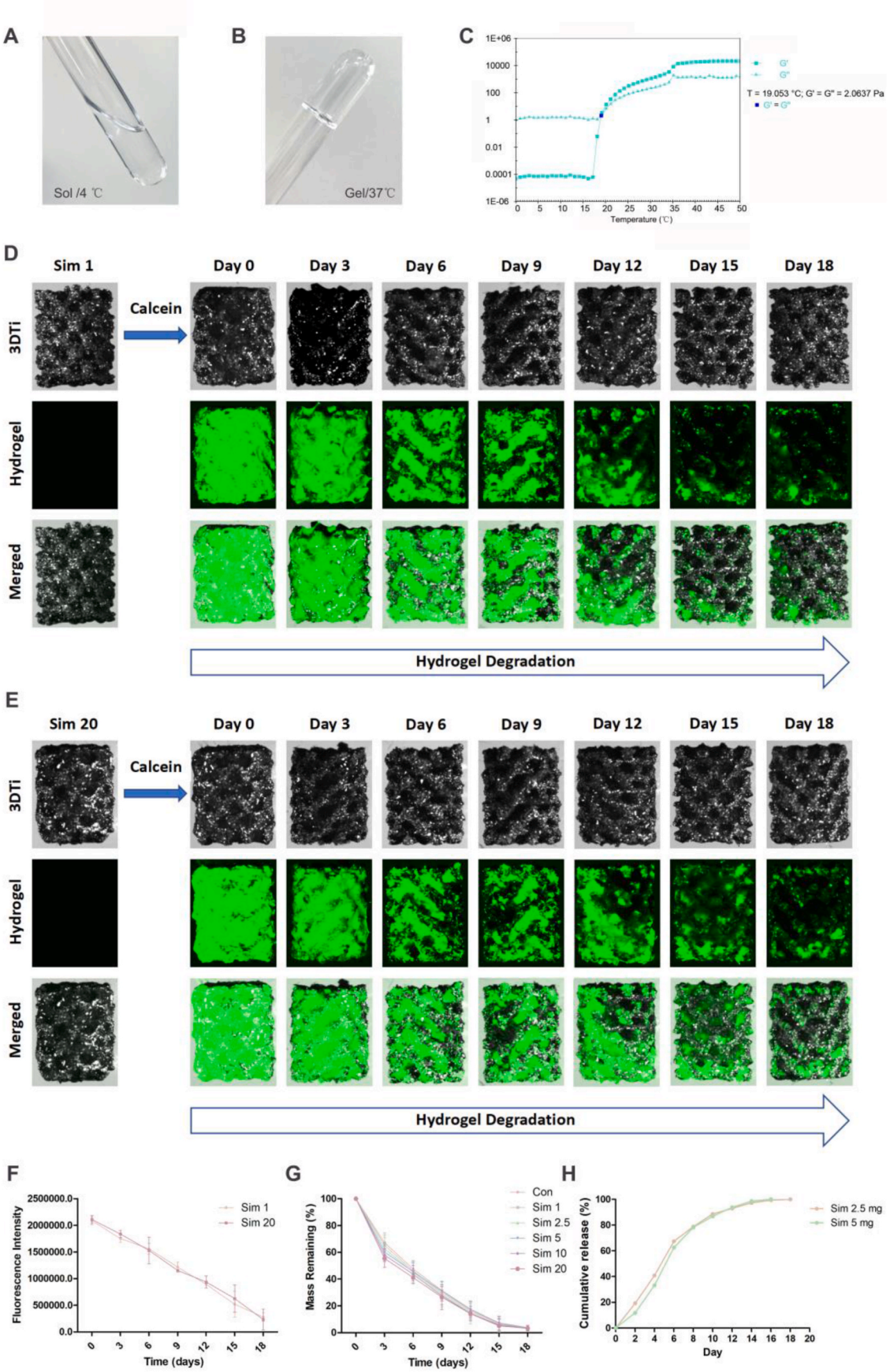

(caption on next page)

Fig. 2. Profiling of Sim-3DTi hydrogel degradation in simulated postsurgical acidic conditions and extracellular microenvironment of tumor cells.
(A) Image of the hydrogels as liquid at 4 °C. (B) Image of the hydrogels as gel at 37 °C. (C) The elastic modulus and viscous modulus of the hydrogel. G′: elastic modulus. G″: viscous modulus. (D–E) Representative hydrogel degradation process in Sim-3DTi loaded with 1 mg/mL or 20 mg/mL simvastatin photographed using stereo microscope. Calcein was added to improve hydrogel visibility. Under 490-nm excitation light, the hydrogel mixed with calcein appears green. The Sim-3DTi hydrogel gradually decreased over 18 days. (F) Change of fluorescence intensity during hydrogel degradation. The fluorescence intensities of images were calculated using Image-Pro Plus 6.0 software. (G) Mass remaining of hydrogel in Sim-3DTi, calculated as the mass of Sim-3DTi at each time point minus that of 3DTi. (H) *In vitro* release profile of simvastatin from the hydrogel. Data are represented as the mean ± standard deviation (SD) (n = 3). $*p < 0.05$, $**p < 0.01$, $***p < 0.001$ compared with control group.

novel Sim-3DTis in this study was an ideal local delivery system for sustained-release of simvastatin, providing a reference for future *in vitro* and *in vivo* experiments.

3.2. There is a rational simvastatin concentration for Sim-3DTi to achieve optimal bio-safety and anti-osteosarcoma in vitro

By co-culturing L929 and 143B cells with Sim-3DTi at different

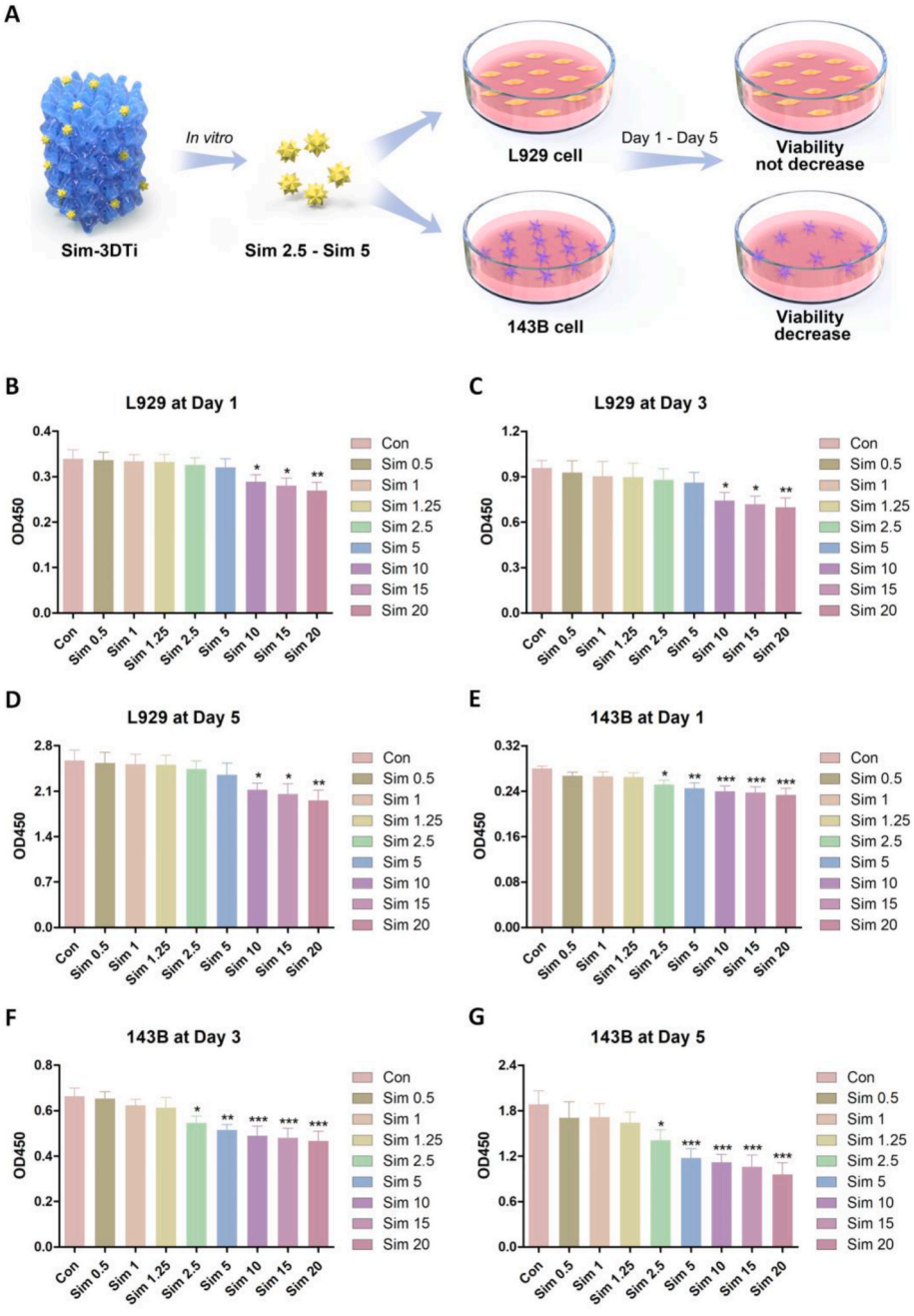

Fig. 3. Simvastatin concentration screening for optimal bio-safety and anti-osteosarcoma effect of Sim-3DTi *in vitro*.
(A) Schematic diagram of biosafety and anti-osteosarcoma effect of Sim-3DTi with optimal simvastatin concentration. Sim-3DTi loaded with 2.5–5 mg/mL simvastatin can reduce osteosarcoma cell viability while not decreasing L929 cell viability at days 1–5. (B–G) Cell viability of L929 and 143B cells at days 1, 3, and 5 after co-culture with Sim-3DTi. Cell viability was quantified using CCK-8 assays at optical density $(OD)_{450}$ (Con: control; Sim: simvastatin).

concentrations, we found that there is an optimal dose range (2.5–5 mg/mL) for simvastatin loading, which can reduce the osteosarcoma cell viability while not decreasing the viability of L929 cells (Fig. 3A). In detail, L929 cell viability did not decrease significantly after co-culture with Sim-3DTi containing simvastatin less than or equal to 5 mg/mL for one (Fig. 3B), three (Fig. 3C) or five days (Fig. 3D). Sim-3DTi could significantly reduce L929 cell viability at simvastatin loading doses ≥10 mg/mL. Therefore, the safe simvastatin loading dose of Sim-3DTi should be ≤ 5 mg/mL. Using the same method, it can be concluded that only when the loading dose of simvastatin is ≥ 2.5 mg/mL, Sim-3DTi can significantly reduce osteosarcoma cell viability after one, three, and five days. These results indicate that in order to ensure the bio-safety and anti-osteosarcoma effect of Sim-3DTi, its simvastatin loading should be 2.5–5 mg/mL.

3.3. Sim-3DTi suppressed osteosarcoma growth but did not affect major organs in vivo

To illustrate its optimal anti-osteosarcoma effect and biosafety *in vivo*, Sim-3DTi loaded with 2.5 mg/mL or 5 mg/mL simvastatin was implanted peritumorally into an osteosarcoma-bearing nude mouse model. As shown in Fig. 4A, with increased simvastatin loading in Sim-3DTi, tumor volume decreased significantly. There was an approximately 59 % decrease ($p < 0.05$) of tumor volume in the Sim 2.5 group (498 ± 106 mm^3) versus the control group (1212 ± 333 mm^3), and the Sim 5 group (274 ± 125 mm^3) showed an approximately 77 % volume decrease compared with the control group ($p < 0.05$) (Fig. 4B). These results were reflected by similar reductions in tumor weight (Fig. 4C), indicating that simvastatin loading can effectively inhibit osteosarcoma growth. However, there was no difference in the body weights of the nude mice (Fig. 4D and E) among the groups.

In order to evaluate the destruction of tumor tissues of simvastatin *in*

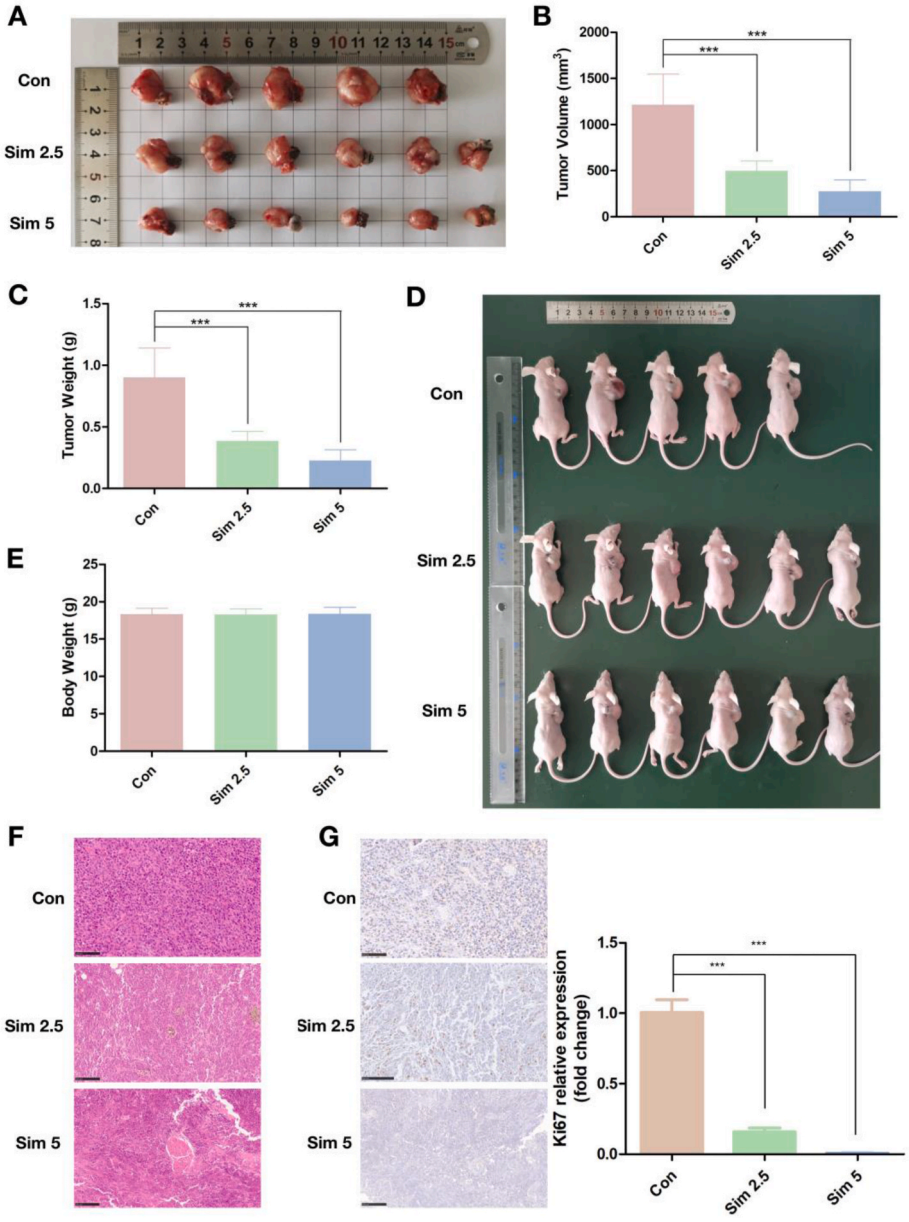

Fig. 4. Anti-osteosarcoma effect and bio-safety of rational-dose simvastatin loading *in vivo*.
Tumor volume (A and B), tumor weight (C), and body weight (D and E) were measured in the control, Sim 2.5, and Sim 5 groups. (F) H&E staining of tumors of nude mice. (E) IHC for Ki67 of tumors of nude mice. Data are represented as the mean ± SD (n = 6). *$p < 0.05$, **$p < 0.01$, ***$p < 0.001$ compared with control group.

vivo, tumor tissues in each group were sectioned and stained with H&E. As shown in Fig. 4F, several necrosis areas were observed in tumor tissues in Sim 2.5 and Sim 5 group, while absent in control group. Moreover, the percentage of necrotic area in Sim 5 group was significantly higher than that in Sim 2.5 group, which inferred more efficient tumor-killing effect of Sim 5. In addition, Ki-67 was one of the representative marker of proliferative potential of osteosarcomas [42]. Moreover, the expression of Ki-67, a representative marker of proliferative potential of osteosarcomas in tumor tissues were assessed (Fig. 4G). The results indicated that the expression level of Ki67 was significantly reduced in Sim 2.5 and Sim 5 group in contrast with control group. Similarly, Sim 5 group exhibited more remarkable suppression effect.

In addition, we revealed that simvastatin did not affect the organization of the major organs, including liver, kidney, heart, lung, and spleen in nude mice by H&E staining. No cell degeneration or necrosis was observed in any group (Fig. S1). These results demonstrated that Sim-3DTi can exert an anti-osteosarcoma effect while maintaining biosafety.

3.4. Sim-3DTi improved the osteogenic effect of 3DTi in vivo

We previously found that simvastatin promoted osteoblast differentiation with upregulated OCN and OPN expression and increased ALP activity *in vitro* [43]. In this study, a widely accepted animal model of bone defects was used to evaluate the osteogenic effects of Sim-3DTi *in vivo* (Fig. 5A). Femur specimens of rabbits implanted with 3DTi (control group) and Sim-3DTi (Sim 2.5 and Sim 5 groups) were harvested four weeks after surgery and then subjected to micro-CT analysis, undecalcified bone histology, and BMP-2 expression evaluation.

Micro-CT reconstruction (Fig. 5A, top row) and sectioning (Fig. 5A, bottom row) revealed osteogenesis was exhibited directly in and around the implants. As shown in Fig. 5A, the yellow part in the top row and the gray section in the bottom row represent new bone. Osteogenesis in and around the implant increased significantly with simvastatin loading. Two indicators (BV/TV, positively associated with osteogenesis, and Tb. Sp, negatively associated with osteogenesis) were calculated using micro-CT imaging to quantitatively analyze osteogenesis. The value of BV/TV decreased from the Sim 5 group to the Sim 2.5 group and then to the control group, while the trend of Tb. Sp was the opposite (Fig. 5B and C), which indicated that simvastatin loading promoted osteogenesis *in vivo*.

Undecalcified sections subjected to Masson Goldner's trichrome staining were used to evaluate bone in-growth and osseointegration of Sim-3DTi *in vivo*, where mineralized bone tissues were stained green (Fig. 5D). Bone in-growth and osseointegration were quantified based on undecalcified sections. As the loading amount of simvastatin increased from the control group to the Sim 2.5 and Sim 5 groups, the amount of mineralized bone in the pores connected to the struts of the 3DTi grew significantly (Fig. 5D). Meanwhile, the degree of bone in-growth (Fig. 5E) and osseointegration (Fig. 5F) in the region of interest (ROI) were also gradually enhanced, proving the osteogenic effect of the topical delivery of simvastatin to bone defects by 3DTi. These results are consistent with the micro-CT imaging results.

Further, we analyzed the expression of BMP-2 around Sim-3DTi. We found that simvastatin significantly upregulated BMP-2 expression in a dose-dependent manner (Fig. 5G), indicating that locally delivered simvastatin may increase osteogenesis, bone-ingrowth, and osseointegration of 3DTi through enhancing BMP-2 expression.

3.5. Sim-3DTi caused the death of osteosarcoma cells with guaranteed biosafety in vitro

Since concentration screening (Fig. 3) and animal experiments (Figs. 4 and 5) had confirmed that loading 5 mg/mL simvastatin into 3DTi had the strongest osteogenic and anti-osteosarcoma effect while ensuring biosafety, we took Sim 5 as an example to explore the anti-osteosarcoma mechanism of Sim-3DTi in the following study. As shown in Fig. 6A, there was no difference between the viability of L929 cells co-cultured with 3DTi and Sim 5, proving the biosafety of 5 mg/mL simvastatin loading. However, 5 mg/mL simvastatin loading significantly decreased the 143B cell proliferation (Fig. 6B) and migration (Fig. 6C and D), implying that Sim-3DTi had a significant anti-osteosarcoma effect. Calcein-AM/PI double staining also revealed that Sim-3DTi induced osteosarcoma cell death, with more red staining of dead cells and less green staining of live cells observed in 143B cells co-cultured with Sim 5 than in those co-cultured with 3DTi (Fig. 6E). According to the fluorescence intensity analysis, the cell survival rate decreased by 35 % after 5 mg/mL simvastatin loading ($p < 0.05$, Fig. 6F). These results demonstrate that Sim-3DTi exerts anti-osteosarcoma effect by promoting osteosarcoma cell death, but does not cause significant death of normal cells (L929 cells). However, how Sim-3DTi causes osteosarcoma cell death remains to be elucidated.

3.6. Sim-3DTi caused osteosarcoma cell death via ferroptosis by upregulating intracellular TF and NOX2 levels both in vivo and in vitro

To clarify how Sim-3DTi causes osteosarcoma cell death, a total of 3015 differently expressed proteins (DEPs), of which 229 proteins were upregulated and 366 proteins were downregulated in the simvastatin group compared to those in the control group, were identified by iTRAQ-based next-generation proteome sequencing (Fig. 7A). Kyoto Encyclopedia of Genes and Genomes (KEGG) enrichment analysis revealed that DEPs were enriched in ferroptosis-related signaling pathways (Fig. 7B). Gene Ontology (GO) functional analysis also demonstrated that simvastatin loading may cause ferroptosis, because ferroptosis-related biological processes (TF transport) and molecular functions (aldehyde dehydrogenase [NAD(P)+] activity) were among the top 30 upregulated GO terms (Fig. 7C). Further analysis of proteome sequencing revealed that TF and NOX2 were the top two ferroptosis-related DEPs that were significantly upregulated in the simvastatin group compared to those in the control group (Fig. 7D). These results suggest that locally delivered simvastatin induces ferroptosis in osteosarcoma cells by upregulating TF and NOX2 expression, thereby causing osteosarcoma cell death and exerting anti-osteosarcoma activity.

The expression levels of TF and NOX2 were measured *in vitro* and *in vivo* to validate the results of the next-generation proteome sequencing. After co-culturing with 3DTi (control group) and Sim 5 (simvastatin group), 143B cells in the simvastatin group expressed higher levels of TF and NOX2 than those in the control group (Fig. 7E). Western blot (Fig. 7F) and IHC (Fig. 7G–I) analyses of tumor tissues also showed that the expression of TF and NOX2 in the simvastatin group was significantly higher than that in the control group. Therefore, protein detection confirmed the proteomic sequencing results, demonstrating that simvastatin can upregulate TF and NOX2 expression in osteosarcoma.

To further confirm the ferroptosis-promoting effect of simvastatin in osteosarcoma cells and the role of TF and NOX2 in this process, a rescue assay was performed. The knockdown efficiency of siRNA was measured using Western blot. As shown in Fig. 8A–B, TF and NOX2 expression was significantly inhibited by specific siRNAs, proving the effectiveness of the siRNA. Notably, the TF knockdown did not affect NOX2 expression in cells without simvastatin treatment, while TF knockdown reversed NOX2 expression in cells treated with simvastatin (Fig. 8C and D), suggesting that the TF/NOX2 axis was established in the presence of simvastatin. In addition, knockdown of TF or NOX2 reversed simvastatin-induced ferroptosis, including a decrease in cell viability (Fig. 8E and F), decreased migration ability (Fig. 8G and H), mitochondrial shrinkage (Fig. 9A), mitochondrial ferrous ion overload (Fig. 9B and C), decrease of intracellular GSH (Fig. 9D), and increase of intracellular MDA (Fig. 9E) in 143B cells. These results demonstrate that TF and NOX2 play key roles in simvastatin-induced ferroptosis in osteosarcoma.

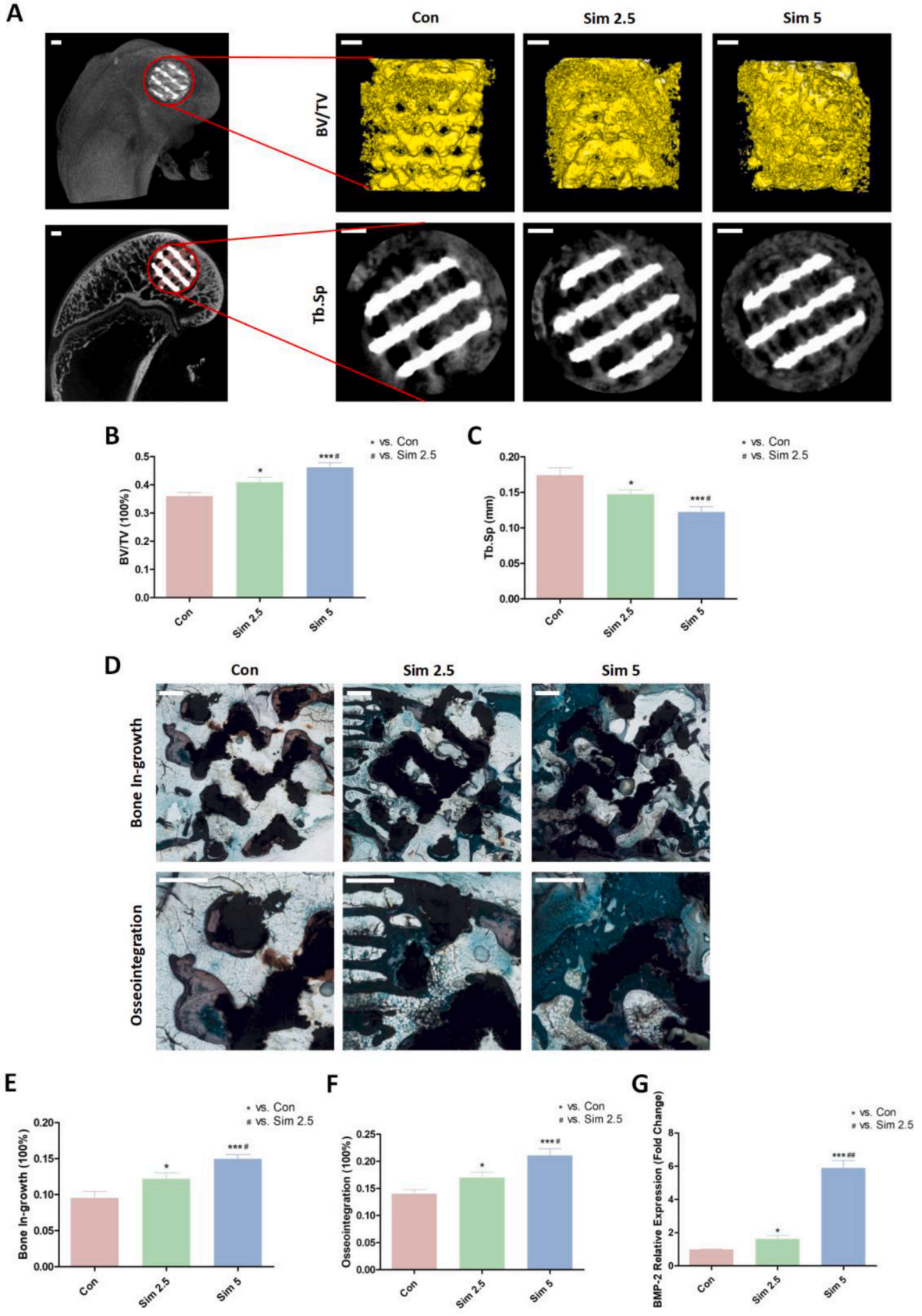

(caption on next page)

Fig. 5. Osteogenic effect of Sim-3DTi *in vivo*.
Four weeks after 3DTi, Sim 2.5, and Sim 5 implant into the bone defect of rabbit femoral condyle, the peripheral 500-μm region around and the intra-porous space within the implant was selected as the region of interest (ROI). (A) Bone and implant in the ROI were reconstructed (top line) and sectioned (bottom line) using micro-CT imaging. The bone and implant were colored yellow and silver, respectively, in the top line, while colored gray and white, respectively, in the bottom line. Osteogenesis in the ROI was quantified by two indicators: bone volume/tissue volume (BV/TV) (B) and trabecular separation (Tb.Sp) (C). (D) Undecalcified histological sections were prepared for all samples, where mineralized bone tissues are stained in green, and the implants appear in black. The quantitative results of bone in-growth (E) and osseointegration (F) were obtained using Image-Pro Plus 6.0 software based on the middle longitudinal sections. (G) The expression of BMP-2 in the new bone around Sim-3DTi was detected by rRT-PCT. Data are represented as the mean ± SD (n = 10). *$p < 0.05$, **$p < 0.01$, ***$p < 0.001$ compared with control group. Scale bars = 1 mm.

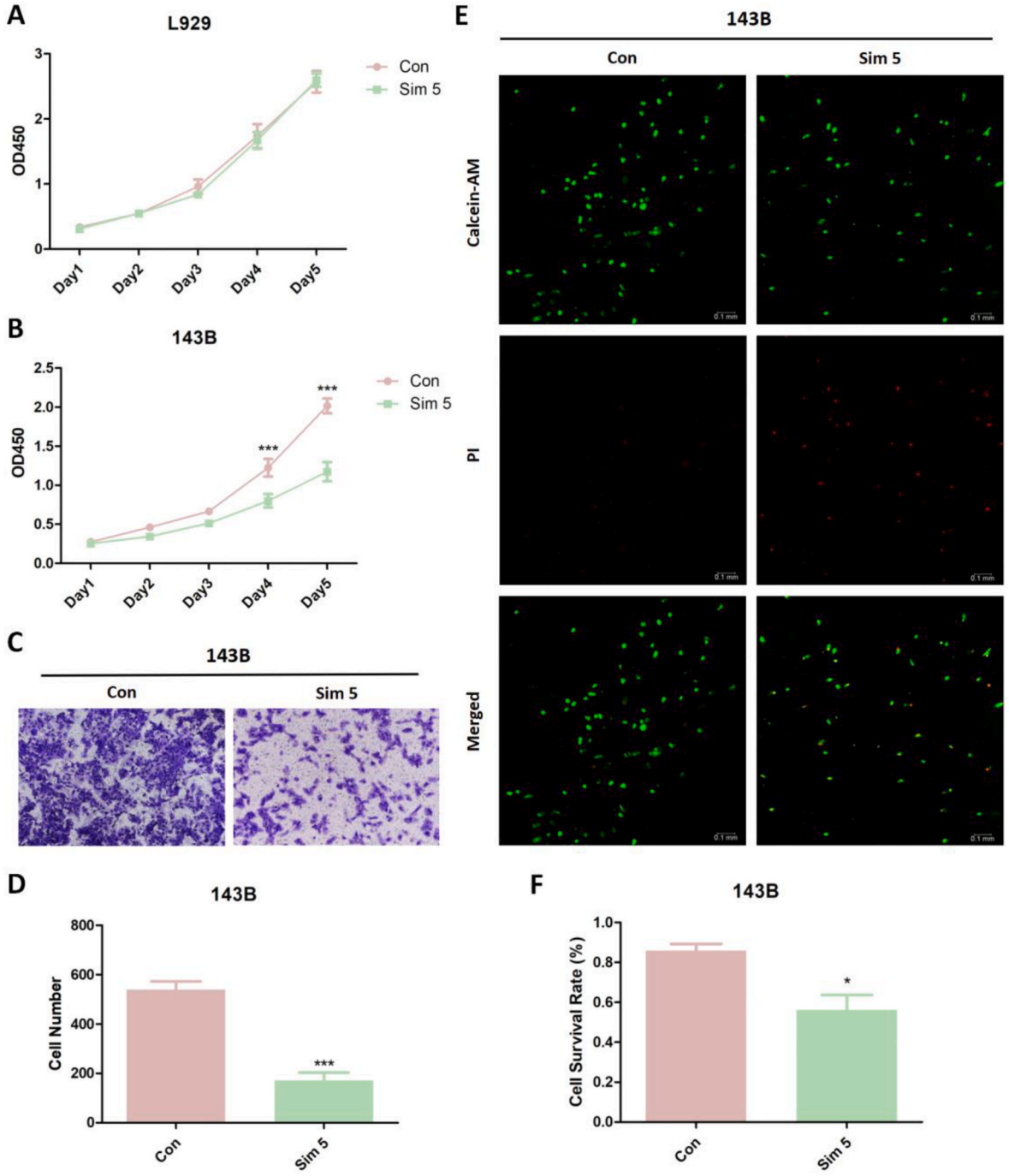

Fig. 6. Effect of Sim-3DTi on proliferation, migration, and survival of osteosarcoma cells *in vitro*.
L929 and 143B cells were co-cultured with 3DTi (control group) or Sim-3DTi with 5 mg/mL simvastatin loading (Sim 5 group) for five days. (A–B) Cell proliferation of L929 and 143B cells quantified using CCK-8 assays at optical density $(OD)_{450}$. (C–D) Migration of 143B cells detected using transwell assays and quantified using cell number counts. (E) Survival of 143B cells shown in representative fluorescence images of calcein-AM/PI staining. The live cells were stained green, and the dead cells were stained red. (F) Quantification of cell survival rate through fluorescence intensities analysis. Data are represented as the mean ± SD (n = 6). *$p < 0.05$, **$p < 0.01$, ***$p < 0.001$ compared with control group.

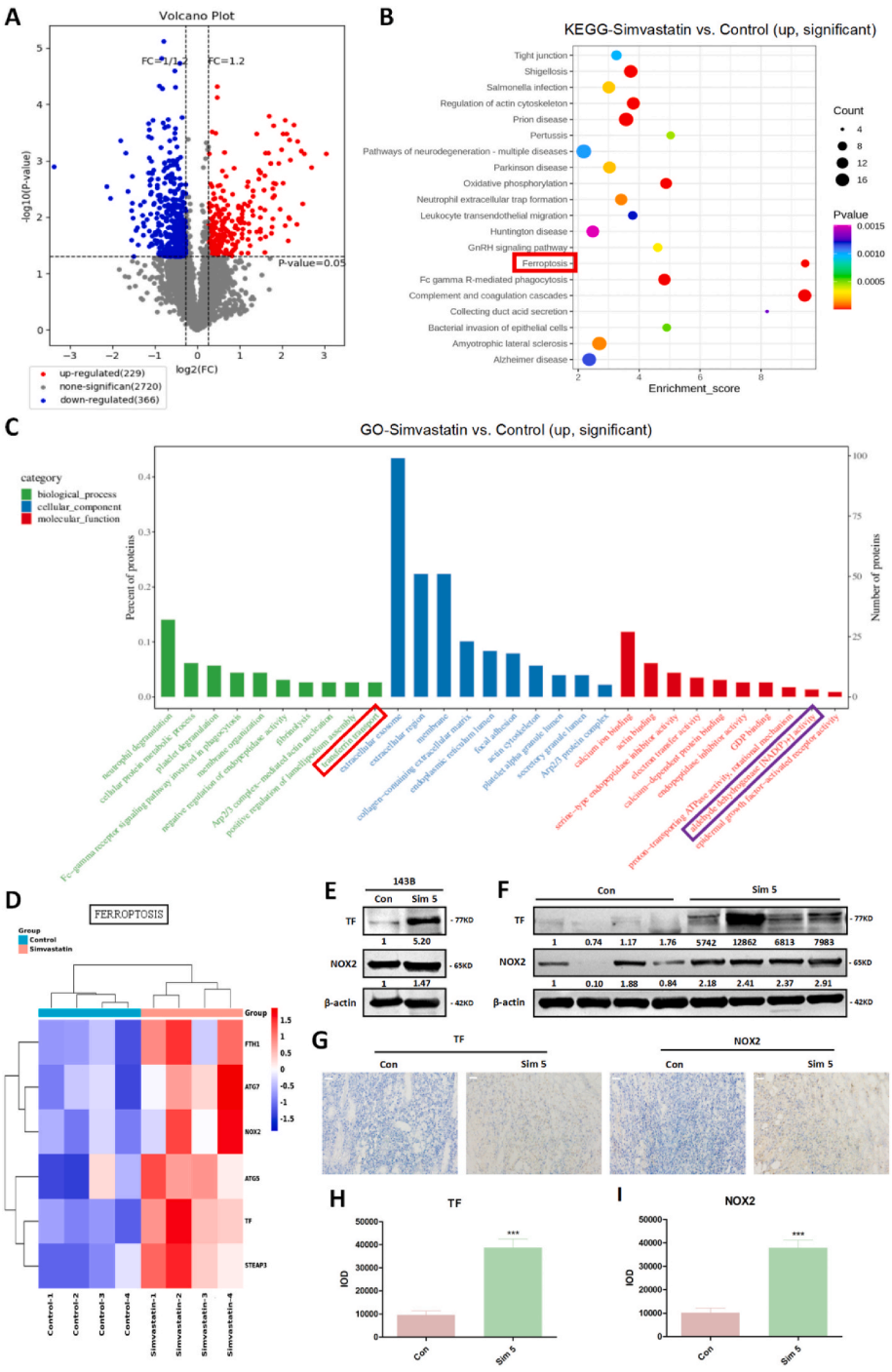

Fig. 7. Simvastatin loading caused the over-expression of ferroptosis-related protein TF and NOX2.
(A–D) Proteome sequencing and bioinformatic analysis of osteosarcoma tissues (simvastatin group vs control group, n = 4). (A) Volcano plot showing the differentially expressed proteins (DEPs). A total of 229 up-regulated proteins (red) and 366 down-regulated proteins (blue) were screened according to the fold change of 1.2 and $p < 0.05$. (B) Representative bubble plot showing the DEP-enriched pathways. The top 20 pathways are listed according to the Kyoto Encyclopedia of Genes and Genomes (KEGG) enrichment score. Bubble sizes are positively correlated with the number of genes enriched. The bubble colors depend on the *p*-value. (C) The top 30 Gene Ontology (GO) terms, including 10 biological processes, 10 cellular components, and 10 molecular functions detected by GO enrichment analysis, in which TF transport and NAD(P) + activity are represented by red and blue squares, respectively. (D) The heat map shows the predicted expression of ferroptosis-related proteins in the DEPs, among which TF and NOX2 are the two proteins with the biggest difference between the simvastatin group and the control group. (E–I) Protein expression of TF and NOX2 after simvastatin treatment *in vitro* and *in vivo*. Protein levels of TF and NOX2 in osteosarcoma cells (E) and tissues (F) were measured using Western blot. The relative integrated gray density is shown under each blot. (G–I) Representative images of immunohistochemistry (IHC) of tumor tissue sections (G) and their quantifications (H–I, n = 10). IOD, integrated optical density. *$p < 0.05$, **$p < 0.01$, ***$p < 0.001$ compared with control group. Scale bars = 10 μm.

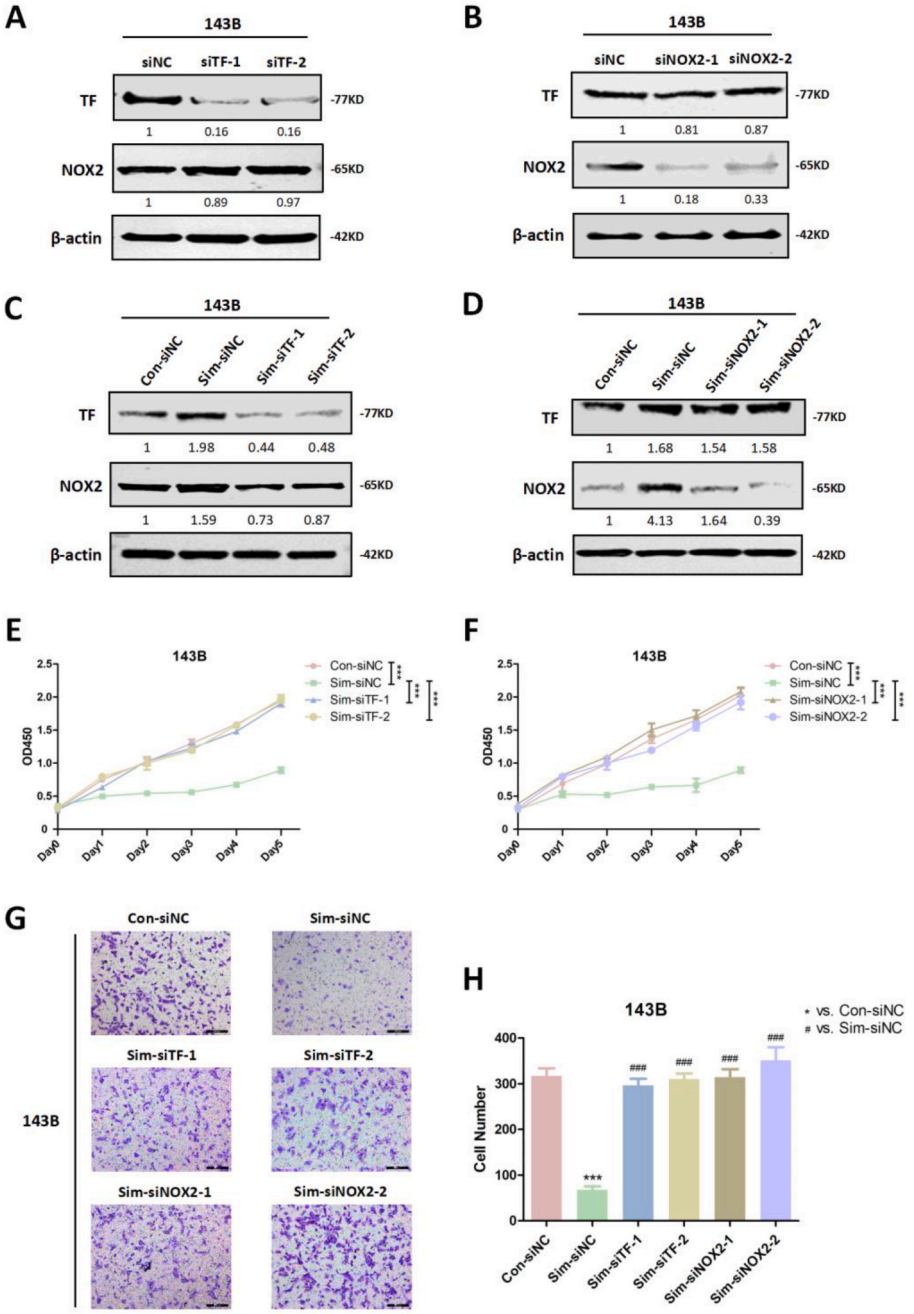

Fig. 8. Knockdown of TF and NOX2 reversed simvastatin-induced cell viability decrease and migration ability reduction of osteosarcoma cells *in vitro*.
(A) Western blot depicting knockdown efficiency of TF siRNA. (B) Western blot depicting knockdown efficiency of NOX2 siRNA. (C) Western blot depicting the effects of simvastatin treatment on TF and NOX2 expression in 143B cells after TF silencing. (D) Western blot depicting the effects of simvastatin treatment on TF and NOX2 expression in 143B cells after NOX2 silencing. The relative integrated gray density of each blot is shown below it. (E) CCK-8 assay results depicting 143B cell proliferation ability after TF silencing. (F) CCK-8 assay results depicting 143B cell proliferation ability after NOX2 silencing. (G–H) Transwell assay results depicting 143B cell migration ability after TF or NOX2 silencing. (Con: control; Sim: simvastatin). (E–F) $^{*}p < 0.05$, $^{**}p < 0.01$, $^{***}p < 0.001$. (G) Scale bars = 200 μm. (H) $^{*}p < 0.05$, $^{**}p < 0.01$, $^{***}p < 0.001$ compared with control group. $^{\#}p < 0.05$, $^{\#\#}p < 0.01$, $^{\#\#\#}p < 0.001$ compared with simvastatin group.

4. Discussion

Since 3DTi was first applied in spinal reconstruction for patients with bone tumors in 2014 [14], many studies have proven its superiority in the repair of bone defects at the joints [44,34], spine [8,45], long bones [8,46,47], and pelvis [8,48]. Compared with traditional bone substitutes, the elastic model of 3DTi bears a closer resemblance to cortical bone, with a larger contact area with the host bone, a more flexible shape design, and no need for bone grafting or second-phase removal. Therefore, the stress shielding and the pressure on the host bone are lesser (the spinal end plate collapse rate is lower), and it is more suitable for the repair of large-span, long-segment, and asymmetric bone defects [8]. However, owing to the increased life expectancy of patients who suffer from bone tumors and are treated with 3DTi, many problems remain to be addressed, such as the increased risk of fatigue breaks and local tumor recurrence [4,5]. Therefore, it is imperative to functionalize 3DTi with osteogenic and anti-tumor properties [49].

Drug loading using the intrinsic porous structure of 3DTi is the most important functionalization method. Compared to coating technology, drug loading can obtain a higher local drug concentration because it

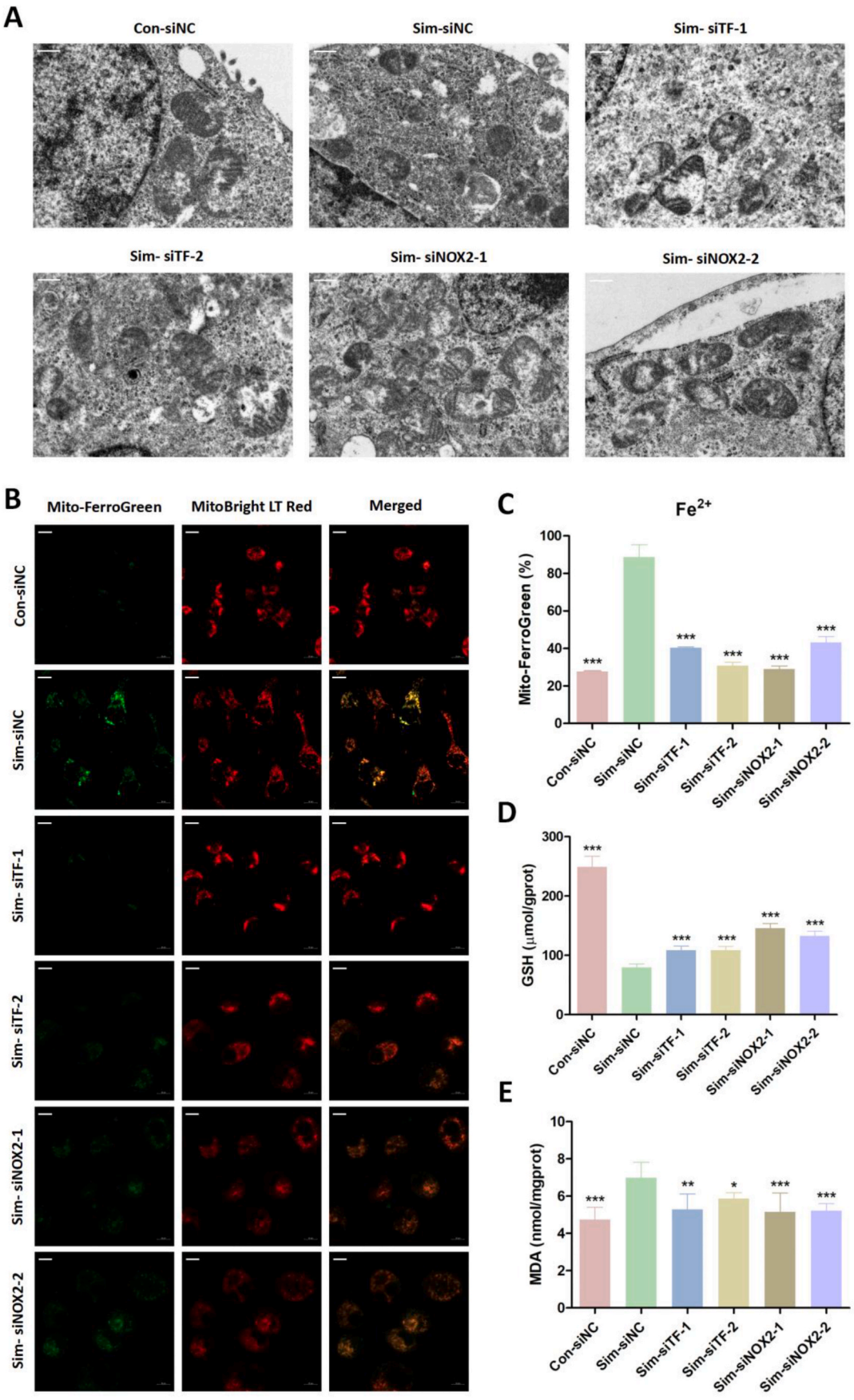

(caption on next page)

Fig. 9. Knockdown of TF and NOX2 reversed simvastatin-induced mitochondrial shrinkage, mitochondrial ferrous ion overload, intracellular GSH decrease, and intracellular MDA increase of osteosarcoma cells *in vitro*
(A) Photographs of mitochondria acquired using transmission electron microscopy. Simvastatin-caused mitochondrial shrinkage was reversed by TF and NOX2 knockdown using specific siRNA. Scale bars = 500 nm. (B) Detection of ferrous irons in mitochondria using a confocal laser scanning microscope. Mitochondria were dyed red while iron ions in the mitochondria were dyed green. Mitochondrial ferrous ions overload was reversed by TF and NOX2 knockdown using specific siRNA. Scale bars = 10 μm. (C) The relative content of ferrous ions in mitochondria was calculated based on the intensity of fluorescence using Image-Pro Plus 6.0 software (n = 3). (D–E) Intracellular glutathione (GSH) and malondialdehyde (MDA) (n = 3). The addition of simvastatin reduced GSH and increased MDA significantly, which was reversed by TF and NOX2 knockdown using corresponding siRNAs. $^{*}p < 0.05$, $^{**}p < 0.01$, $^{***}p < 0.001$ compared with simvastatin group.

makes better use of the internal space of 3DTi rather than only its surface. Thus, it is more suitable for tumor treatments, which often require higher drug concentrations [49]. Although growth factors (such as recombinant human BMP-2 (rhBMP-2) [15] and stromal cell-derived factor 1 (SDF-1) α [50]) and simvastatin [18] have been used to promote osteogenesis around 3DTi in animal models, no studies have demonstrated both anti-tumor and osteogenic effects through drug loading. To the best of our knowledge, this is the first preclinical study to achieve both anti-tumor and osteogenic functionalization of 3DTi using single-drug loading.

The osteogenic and anti-tumor effects of simvastatin have been described separately in previous studies; however, the administration methods and measurements vary considerably, and the results are not consistent. One clinical trial showed that oral simvastatin has an anti-tumor effect, but its effect was not obvious and can only be observed in large sample size [51]. Animal studies have demonstrated that simvastatin administered alone either orally or intravenously does not significantly inhibit osteosarcoma tumor growth [52,53]. Therefore, oral simvastatin is not a feasible anti-tumor agent. A previous study reported the normalization of tumor vessels and reduction of tumor burden in a nude mouse model using an intraosseous injection of simvastatin [54]. It has also been reported that loading simvastatin into 3DTi results in osteogenic activity in a tibial defect rabbit model [18]. However, it is unclear whether Sim-3DTi can suppress tumors and promote osteogenesis.

Prior to animal experiments, Sim-3DTi's drug loading capacity, drug release rate and reasonable drug loading concentration were carefully studied. Consistent a previous study [17], we found that regardless of the simvastatin loading concentration, the release time was approximately 18 days (Fig. 2), and 5 mg/mL was the optimal *in vitro* concentration for anti-osteosarcoma effects while ensuring biosafety (Fig. 3). However, *in vitro* experiments can only preliminarily screen the reasonable drug loading concentration of Sim-3DTi, and the anti-osteosarcoma and bone promoting effects of Sim-3DTi needed to be further verified using animal experiments.

To simultaneously verify the osteogenic and anti-tumor effects of Sim-3DTi, an animal model of bone tumors with critical bone defects is ideal. However, in animals that are commonly used to model critical bone defects, such as rats, rabbits, and sheep, human cancer cells cannot survive because interspecies differences mean animal models often ultimately reject human cancer cells. For tumor-bearing animals such as nude mice, the bone is too small to accommodate 3DTi and the bone mass is lower than that in normal mice [55]. Therefore, in this study, two animal models (a nude mouse tumor-bearing model and a rabbit bone defect model) were used to evaluate the anti-osteosarcoma (Fig. 4) and osteogenic (Fig. 5) effects of Sim-3DTi separately. The evaluation results showed that both 2.5 mg/mL and 5 mg/mL simvastatin played a significant role in reducing the osteosarcoma burden and promoting osteogenesis without obvious side effects. Thus, Sim-3DTi with rational-dose simvastatin loading is a bone substitute with a transformation potential that can be used to treat osteosarcoma-associated bone defects.

Because simvastatin is a multitarget drug, its anti-tumor mechanisms are complex. Different modes of administration and drug concentrations may produce different anti-tumor mechanisms [56]. In this study, we found a new anti-tumor mechanism of simvastatin, which is closely related to ferroptosis and the ferroptosis-related proteins TF and NOX2 (Figs. 6–9). Transferrin is an iron-carrier protein essential for ferroptosis [57], and NOX2 transports electrons across the plasma membrane to produce superoxide and downstream ROS, which promote lipid peroxidation during ferroptosis [58–62]. We showed that simvastatin upregulated TF and NOX2 expression in osteosarcoma cells, whereas silencing TF or NOX2 using siRNAs reversed simvastatin-induced ferroptosis, indicating that simvastatin led to ferroptosis in osteosarcoma cells by upregulating TF and NOX2. To the best of our knowledge, the present study is the first to demonstrate that simvastatin has anti-tumor effects by causing ferroptosis in tumors beyond breast and endometrial cancers [63–65]. This is also the first study to demonstrate that simvastatin activates both TF and NOX2 to induce ferroptosis.

Multitarget drugs often have multiple functions that are accompanied by side effects. Prevention of the side effects of drug therapy is a current research hotspot. Most studies attempt to render a drug more target specific by changing the structure or adding a drug carrier; however, these methods are complex, and it is difficult to achieve clinical transformation. In a previous study, it was found that loading chemotherapeutic drugs into the 3DTi pores to achieve local drug application could have a better anti-tumor effect and fewer side effects than traditional intravenous administration [15], suggesting that local insertion of implants is a more efficient method of drug administration. However, chemotherapeutic agents may have an inhibitory effect on 3DTi peripheral osteogenesis [17]. This study used the same method to apply simvastatin to bone tumor treatment, where simvastatin also played a role in promoting osteogenesis by increasing BMP-2 expression, as previously reported [66–68]. Therefore, Sim-3DTi has a clear anti-osteosarcoma and osteogenic mechanisms and can meet the needs of tumor-related bone defects (Fig. 10). As loading simvastatin into 3DTi is simple and practical, and all raw materials are safe for use in the human body, Sim-3DTi has a good translational value.

5. Conclusions

In this study, we used the thermosensitive PLGA-PEG-PLGA hydrogel to load simvastatin into 3DTi, thereby constructing a simvastatin/hydrogel-loaded complex, namely Sim-3DTi. Simvastatin in Sim-3DTi can be released for over 18 days with hydrogel degradation. By co-culturing L929 and 143B cells with Sim-3DTi at different concentrations, we found that there was a rational simvastatin concentration (2.5–5 mg/mL) for Sim-3DTi to achieve optimal bio-safety and anti-osteosarcoma. In the bone defect model of rabbit condyles and the osteosarcoma-bearing model of nude mice, Sim-3DTi with rational simvastatin concentration loading could upregulate BMP-2 expression, increase osteogenesis and suppress osteosarcoma while ensuring good biosafety. By proteomic sequencing, bioinformatics analysis, and *in vivo* and *in vitro* verification, we proved that locally delivered simvastatin could induce ferroptosis of osteosarcoma cells by upregulating TF/NOX2 expression, thus playing an anti-osteosarcoma role. As Sim-3DTi is simple to construct and presents good biosafety and clear osteogenic and anti-osteosarcoma activities, it should be a promising bone substitute for repairing osteosarcoma-related critical bone defects.

Funding

This work was supported by National Natural Science Foundation of China (grant number 82272456 and 82202748) and China Postdoctoral

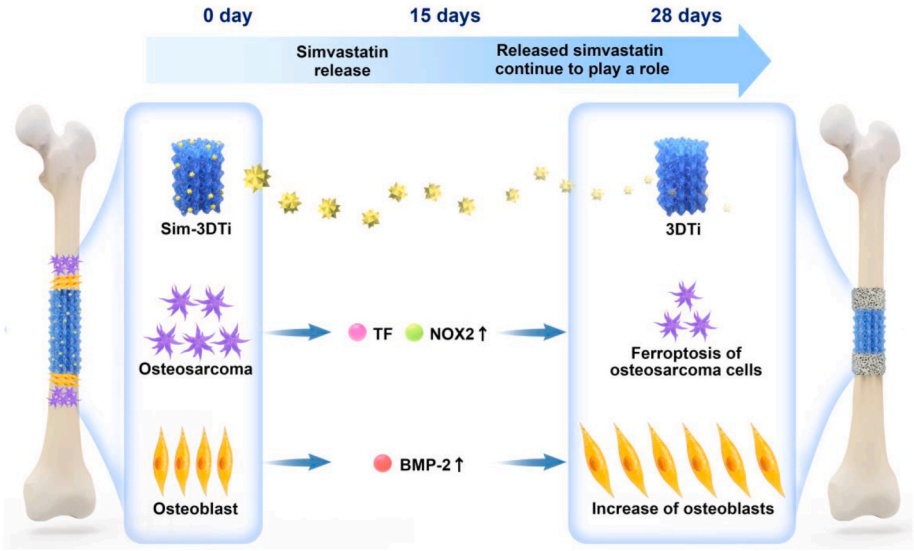

Fig. 10. Anti-osteosarcoma and osteogenic mechanisms of Sim-3DTi.

Science Foundation (grant number 2022M720297).

Ethics approval statement

All animal experimental protocols were approved by the Peking University Institutional Review Board on Biomedical Ethics in the Care and Use of Laboratory Animals (Project Number: LA2020465).

CRediT authorship contribution statement

Zehao Jing: Formal analysis, Investigation, Methodology, Visualization, Writing – original draft, Data curation, Funding acquisition, Software. **Wanqiong Yuan:** Data curation, Formal analysis, Investigation, Methodology, Software, Visualization, Writing – original draft. **Jiedong Wang:** Data curation, Formal analysis, Investigation, Methodology, Software, Visualization, Writing – original draft. **Renhua Ni:** Formal analysis, Methodology, Visualization. **Yu Qin:** Data curation, Investigation. **Zhinan Mao:** Investigation, Methodology. **Feng Wei:** Formal analysis, Validation, Writing – review & editing. **Chunli Song:** Formal analysis, Validation, Writing – review & editing. **Yufeng Zheng:** Conceptualization, Writing – review & editing. **Hong Cai:** Conceptualization, Funding acquisition, Resources, Writing – review & editing. **Zhongjun Liu:** Conceptualization, Project administration, Supervision, Writing – review & editing.

Declaration of competing interest

Yufeng Zheng is an editorial board member/editor-in-chief for Bioactive Materials and was not involved in the editorial review or the decision to publish this article. All authors declare that there are no competing interests.

Acknowledgement

The authors would like to acknowledge the research support from Beijing AKEC Medical Co., Ltd. and the guidance of Kuo Zhang for the animal experiments.

Appendix A. Supplementary data

Supplementary data to this article can be found online at https://doi.org/10.1016/j.bioactmat.2023.11.001.

References

[1] Z.Y. Jiang, J.B. Liu, X.F. Wang, Y.S. Ma, D. Fu, Current status and prospects of clinical treatment of osteosarcoma, Technol. Cancer Res. Treat. 21 (2022), 15330338221124696, https://doi.org/10.1177/15330338221124696.
[2] S. Ferrari, P. Ruggieri, G. Cefalo, A. Tamburini, R. Capanna, F. Fagioli, A. Comandone, R. Bertulli, G. Bisogno, E. Palmerini, M. Alberghini, A. Parafioriti, A. Linari, P. Picci, G. Bacci, Neoadjuvant chemotherapy with methotrexate, cisplatin, and doxorubicin with or without ifosfamide in nonmetastatic osteosarcoma of the extremity: an Italian sarcoma group trial ISG/OS-1, J. Clin. Oncol. 30 (2012) 2112–2118, https://doi.org/10.1200/JCO.2011.38.4420.
[3] A.K. Ozturk, Z.L. Gokaslan, J.P. Wolinsky, Surgical treatment of sarcomas of the spine, Curr. Treat. Options Oncol. 15 (2014) 482–492, https://doi.org/10.1007/s11864-014-0290-8.
[4] N. Omer, M.C. Le Deley, S. Piperno-Neumann, P. Marec-Berard, A. Italiano, N. Corradini, C. Bellera, L. Brugières, N. Gaspar, Phase-II trials in osteosarcoma recurrences: a systematic review of past experience, Eur. J. Cancer 75 (2017) 98–108, https://doi.org/10.1016/j.ejca.2017.01.005.
[5] E. Simpson, H.L. Brown, Understanding osteosarcomas, Off. J. Am. Acad. Physician Assistants (JAAPA) 31 (2018) 15–19, https://doi.org/10.1097/01.JAA.0000541477.24116.8d.
[6] M.E. Anderson, Update on survival in osteosarcoma, Orthop. Clin. N. Am. 47 (2016) 283–292, https://doi.org/10.1016/j.ocl.2015.08.022.
[7] J. Liao, R. Han, Y. Wu, Z. Qian, Review of a new bone tumor therapy strategy based on bifunctional biomaterials, Bone Res 9 (2021) 18, https://doi.org/10.1038/s41413-021-00139-z.
[8] T. Zhang, Q. Wei, H. Zhou, Z. Jing, X. Liu, Y. Zheng, H. Cai, F. Wei, L. Jiang, M. Yu, Y. Cheng, D. Fan, W. Zhou, X. Lin, H. Leng, J. Li, X. Li, C. Wang, Y. Tian, Z. Liu, Three-dimensional-printed individualized porous implants: a new "implant-bone" interface fusion concept for large bone defect treatment, Bioact. Mater. 6 (2021) 3659–3670, https://doi.org/10.1016/j.bioactmat.2021.03.030.
[9] B. Tan, Q. Tang, Y. Zhong, Y. Wei, L. He, Y. Wu, J. Wu, J. Liao, Biomaterial-based strategies for maxillofacial tumour therapy and bone defect regeneration, Int. J. Oral Sci. 13 (1) (2021 Mar 16) 9, https://doi.org/10.1038/s41368-021-00113-9.
[10] J. Liao, K. Shi, Y. Jia, Y. Wu, Z. Qian, Gold nanorods and nanohydroxyapatite hybrid hydrogel for preventing bone tumor recurrence via postoperative photothermal therapy and bone regeneration promotion, Bioact. Mater. 6 (8) (2021 Jan 22) 2221–2230, https://doi.org/10.1016/j.bioactmat.2021.01.006.
[11] S. Cleemput, S.E.F. Huys, R. Cleymaet, W. Cools, M.Y. Mommaerts, Additively manufactured titanium scaffolds and osteointegration - meta-analyses and moderator-analyses of in vivo biomechanical testing, Biomater. Res. 25 (2021) 18, https://doi.org/10.1186/s40824-021-00216-8.
[12] S. Barui, S. Chatterjee, S. Mandal, A. Kumar, B. Basu, Microstructure and compression properties of 3D powder printed Ti-6Al-4V scaffolds with designed porosity: experimental and computational analysis, Mater. Sci. Eng., C 70 (2017) 812–823, https://doi.org/10.1016/j.msec.2016.09.040.
[13] F. Wei, Z. Li, Z. Liu, X. Liu, L. Jiang, M. Yu, N. Xu, F. Wu, L. Dang, H. Zhou, Z. Li, H. Cai, Upper cervical spine reconstruction using customized 3D-printed vertebral body in 9 patients with primary tumors involving C2, Ann. Transl. Med. 8 (2020) 332, https://doi.org/10.21037/atm.2020.03.32.
[14] N. Xu, F. Wei, X. Liu, L. Jiang, H. Cai, Z. Li, M. Yu, F. Wu, Z. Liu, Reconstruction of the Upper Cervical Spine Using a Personalized 3D-Printed Vertebral Body in an Adolescent with Ewing Sarcoma, vol. 41, Phila Pa 1976, Spine, 2016, pp. E50–E54, https://doi.org/10.1097/BRS.0000000000001179.
[15] T. Zhang, Q. Wei, D. Fan, X. Liu, W. Li, C. Song, Y. Tian, H. Cai, Y. Zheng, Z. Liu, Improved osseointegration with rhBMP-2 intraoperatively loaded in a specifically

designed 3D-printed porous Ti6Al4V vertebral implant, Biomater. Sci. 8 (2020) 1279–1289, https://doi.org/10.1039/c9bm01655d.
[16] J. Lv, P. Xiu, J. Tan, Z. Jia, H. Cai, Z. Liu, Enhanced angiogenesis and osteogenesis in critical bone defects by the controlled release of BMP-2 and VEGF: implantation of electron beam melting-fabricated porous Ti6Al4V scaffolds incorporating growth factor-doped fibrin glue, Biomed. Mater. 10 (2015), 035013, https://doi.org/10.1088/1748-6041/10/3/035013.
[17] Z.H. Jing, R.H. Ni, J.D. Wang, X.H. Lin, D.Y. Fan, Q.G. Wei, T. Zhang, Y.F. Zheng, H. Cai, Z.J. Liu, Practical strategy to construct anti-osteosarcoma bone substitutes by loading cisplatin into 3D-printed titanium alloy implants using a thermosensitive hydrogel, Bioact. Mater. 6 (2021) 4542–4557, https://doi.org/10.1016/j.bioactmat.2021.05.007.
[18] H. Liu, W. Li, C. Liu, J. Tan, H. Wang, B. Hai, H. Cai, H.J. Leng, Z.J. Liu, C.L. Song, Incorporating simvastatin/poloxamer 407 hydrogel into 3D-printed porous Ti6Al4V scaffolds for the promotion of angiogenesis, osseointegration and bone ingrowth, Biofabrication 8 (2016), 045012, https://doi.org/10.1088/1758-5090/8/4/045012.
[19] H. Jin, Y. Ji, Y. Cui, L. Xu, H. Liu, J. Wang, S.-I. Simvastatin-incorporated drug delivery systems for bone regeneration, ACS Biomater. Sci. Eng. 7 (2021) 2177–2191, https://doi.org/10.1021/acsbiomaterials.1c00462.
[20] T. Sun, J. Huang, W. Zhang, X. Zheng, H. Wang, J. Liu, H. Leng, W. Yuan, C. Song, Simvastatin-hydroxyapatite coatings prevent biofilm formation and improve bone formation in implant-associated infections, Bioact. Mater. 21 (2022 Aug 13) 44–56, https://doi.org/10.1016/j.bioactmat.2022.07.028.
[21] P. Bergman, C. Linde, K. Pütsep, A. Pohanka, S. Normark, B. Henriques-Normark, J. Andersson, L. Björkhem-Bergman, Studies on the antibacterial effects of statins–in vitro and in vivo, PLoS One 6 (8) (2011), e24394, https://doi.org/10.1371/journal.pone.0024394.
[22] S. Kany, M. Woschek, N. Kneip, R. Sturm, M. Kalbitz, M. Hanschen, B. Relja, Simvastatin exerts anticancer effects in osteosarcoma cell lines via geranylgeranylation and c-Jun activation, Int. J. Oncol. 52 (2018) 1285–1294, https://doi.org/10.3892/ijo.2018.4288.
[23] A. Mangelinck, N. Habel, A. Mohr, N. Gaspar, B. Stefanovska, O. Fromigué, Synergistic anti-tumor effect of simvastatin combined to chemotherapy in osteosarcoma, Cancers 13 (2021), https://doi.org/10.3390/cancers13225869.
[24] W.A. Kamel, E. Sugihara, H. Nobusue, S. Yamaguchi-Iwai, N. Onishi, K. Maki, Y. Fukuchi, K. Matsuo, A. Muto, H. Saya, T. Shimizu, Simvastatin-induced apoptosis in osteosarcoma cells: a key role of RhoA-AMPK/p38 MAPK signaling in antitumor activity, Mol. Cancer Therapeut. 16 (2017) 182–192, https://doi.org/10.1158/1535-7163.MCT-16-0499.
[25] P. Dehghankelishadi, M.F. Maritz, N. Dmochowska, P. Badiee, E. Cheah, I. Kempson, R.I. Berbeco, B. Thierry, Formulation of simvastatin within high density lipoprotein enables potent tumour radiosensitisation, J. Contr. Release 346 (2022) 98–109, https://doi.org/10.1016/j.jconrel.2022.04.017.
[26] J.M. Dodda, T. Remiš, S. Rotimi, Y.C. Yeh, Progress in the drug encapsulation of poly(lactic-co-glycolic acid) and folate-decorated poly(ethylene glycol)-poly(lactic-co-glycolic acid) conjugates for selective cancer treatment, J. Mater. Chem. B 10 (2022) 4127–4141, https://doi.org/10.1039/d2tb00469k.
[27] Z. Azhari, P. Smith, S. McMahon, W. Wang, R.E. Cameron, Modulating drug release from short poly(ethylene glycol) block initiated poly(L-lactide) di-block copolymers, Pharm. Res. (N. Y.) (2022), https://doi.org/10.1007/s11095-022-03228-8.
[28] N. Xu, X. Zhang, T. Qi, Y. Wu, X. Xie, F. Chen, D. Shao, J. Liao, Biomedical applications and prospects of temperature-orchestrated photothermal therapy, MedComm-Biomaterials and Applications (2022), e25, https://doi.org/10.1002/mba2.25.
[29] B.O. Grabarek, D. Boron, E. Morawiec, P. Michalski, V. Palazzo-Michalska, L. Pach, B. Dziuk, M. Swider, N. Zmarzly, Crosstalk between statins and cancer prevention and therapy: an update, Pharmaceuticals 14 (2021) 1220, https://doi.org/10.3390/ph14121220.
[30] H. Terzi, A. Altun, M. Şencan, In vitro comparison of the cytotoxic effects of statins on U266 myeloma cell line, Indian J. Med. Res. 150 (2019) 630–634, https://doi.org/10.4103/ijmr.IJMR_672_18.
[31] Y. Sun, Z. Xue, T. Huang, X. Che, G. Wu, Lipid metabolism in ferroptosis and ferroptosis-based cancer therapy, Front. Oncol. 12 (2022), 941618, https://doi.org/10.3389/fonc.2022.941618.
[32] X. Chen, R. Kang, G. Kroemer, D. Tang, Broadening horizons: the role of ferroptosis in cancer, Nat. Rev. Clin. Oncol. 18 (2021) 280–296, https://doi.org/10.1038/s41571-020-00462-0.
[33] G. Lei, L. Zhuang, B.Y. Gan, Targeting ferroptosis as a vulnerability in cancer, Nat. Rev. Cancer 22 (2022) 381–396, https://doi.org/10.1038/s41568-022-00459-0.
[34] H. Ma, C. He, Y. Cheng, D. Li, Y. Gong, J. Liu, H. Tian, X. Chen, PLK1shRNA and doxorubicin co-loaded thermosensitive PLGA-PEG-PLGA hydrogels for osteosarcoma treatment, Biomaterials 35 (2014) 8723–8734, https://doi.org/10.1016/j.biomaterials.2014.06.045.
[35] P.S. Chan, J.W. Xian, Q. Li, C.W. Chan, S.S.Y. Leung, K.K.W. To, Biodegradable thermosensitive PLGA-PEG-PLGA polymer for non-irritating and sustained ophthalmic drug delivery, AAPS J. 21 (2019) 59, https://doi.org/10.1208/s12248-019-0326-x.
[36] G. Carlsson, B. Gullberg, L. Hafström, Estimation of liver tumor volume using different formulas - an experimental study in rats, J. Cancer Res. Clin. Oncol. 105 (1983) 20–23, https://doi.org/10.1007/BF00391826.
[37] Y. Li, W. Yang, X. Li, X. Zhang, C. Wang, X. Meng, Y. Pei, X. Fan, P. Lan, C. Wang, X. Li, Z. Guo, Improving osteointegration and osteogenesis of three-dimensional porous Ti6Al4V scaffolds by polydopamine-assisted biomimetic hydroxyapatite coating, ACS Appl. Mater. Interfaces 7 (2015) 5715–5724, https://doi.org/10.1021/acsami.5b00331.
[38] P. Xiu, Z. Jia, J. Lv, C. Yin, Y. Cheng, K. Zhang, C. Song, H. Leng, Y. Zheng, H. Cai, Z. Liu, Tailored surface treatment of 3D printed porous Ti6Al4V by microarc oxidation for enhanced osseointegration via optimized bone in-growth patterns and interlocked bone/implant interface, ACS Appl. Mater. Interfaces 8 (2016) 17964–17975, https://doi.org/10.1021/acsami.6b05893.
[39] P. Mertins, F. Yang, T. Liu, D.R. Mani, V.A. Petyuk, M.A. Gillette, K.R. Clauser, J. W. Qiao, M.A. Gritsenko, R.J. Moore, D.A. Levine, R. Townsend, P. Erdmann-Gilmore, J.E. Snider, S.R. Davies, K.V. Ruggles, D. Fenyo, R.T. Kitchens, S.Q. Li, N. Olvera, F. Dao, H. Rodriguez, D.W. Chan, D. Liebler, F. White, K.D. Rodland, G. B. Mills, R.D. Smith, A.G. Paulovich, M. Ellis, S.A. Carr, Ischemia in tumors induces early and sustained phosphorylation changes in stress kinase pathways but does not affect global protein levels, Mol. Cell. Proteomics 13 (2014) 1690–1704, https://doi.org/10.1074/mcp.M113.036392.
[40] W. Yuan, B. Liu, X. Wang, T. Li, H. Xue, X. Mo, S. Yang, S. Ding, W. Han, CMTM3 decreases EGFR expression and EGF-mediated tumorigenicity by promoting Rab5 activity in gastric cancer, Cancer Lett. 386 (2017) 77–86, https://doi.org/10.1016/j.canlet.2016.11.015.
[41] A. Lopera, J.A. Aguilar, R. Belda, B. Verdejo, J.W. Steed, E. García-España, Hybrid GMP-polyamine hydrogels as new biocompatible materials for drug encapsulation, Soft Matter 16 (2020) 6514–6522, https://doi.org/10.1039/d0sm00704h.
[42] S. Fujiwara, T. Kawamoto, Y. Kawakami, Y. Koterazawa, H. Hara, T. Takemori, K. Kitayama, S. Yahiro, K. Kakutani, T. Matsumoto, T. Matsushita, T. Niikura, M. Koyanagi-Aoi, T. Aoi, R. Kuroda, T. Akisue, Acquisition of cancer stem cell properties in osteosarcoma cells by defined factors, Stem Cell Res. Ther. 11 (1) (2020 Oct 2) 429, https://doi.org/10.1186/s13287-020-01944-9.
[43] C. Song, Z. Guo, Q. Ma, Z. Chen, Z. Liu, H. Jia, G. Dang, Simvastatin induces osteoblastic differentiation and inhibits adipocytic differentiation in mouse bone marrow stromal cells, Biochem. Biophys. Res. Commun. 308 (3) (2003 Aug 29) 458–462, https://doi.org/10.1016/S0006-291X(03)01408-6.
[44] Y. Li, X.G. Wang, H. Tian, Reconstruction for massive proximal tibial bone defects using patient-customized three-dimensional-printed metaphyseal cones in revision total knee arthroplasty, Orthop. Surg. 14 (2022) 1071–1077, https://doi.org/10.1111/os.13282.
[45] H. Zhou, S.S. Liu, Z.H. Li, X.G. Liu, L. Dang, Y. Li, Z.H. Li, P.P. Hu, B. Wang, F. Wei, Z.J. Liu, 3D-printed vertebral body for anterior spinal reconstruction in patients with thoracolumbar spinal tumors, J. Neurosurg. Spine 37 (2022) 1–9, https://doi.org/10.3171/2022.1.SPINE21900.
[46] G. Hou, B. Liu, Y. Tian, Z. Liu, F. Zhou, Reconstruction of ipsilateral femoral and tibial bone defect by 3D printed porous scaffold without bone graft: a case report, JBJS Case Connect 12 (2022), https://doi.org/10.2106/JBJS.CC.20.00592.
[47] G. Hou, B. Liu, Y. Tian, Z. Liu, F. Zhou, H. Ji, Z. Zhang, Y. Guo, Y. Lv, Z. Yang, P. Wen, Y. Zheng, Y. Cheng, An innovative strategy to treat large metaphyseal segmental femoral bone defect using customized design and 3D printed micro-porous prosthesis: a prospective clinical study, J. Mater. Sci. Mater. Med. 31 (2020) 66, https://doi.org/10.1007/s10856-020-06406-5.
[48] H. Liang, W. Guo, X. Tang, R. Yang, T. Yan, Y. Yang, T. Ji, X. Sun, L. Xie, J. Xu, Venous tumor thrombus in primary bone sarcomas in the pelvis: a clinical and radiographic study of 451 cases, J. Bone Joint Surg. Am. 103 (2021) 1510–1520, https://doi.org/10.2106/JBJS.20.00569.
[49] Z. Jing, T. Zhang, P. Xiu, H. Cai, Q. Wei, D. Fan, X. Lin, C. Song, Z. Liu, Functionalization of 3D-printed titanium alloy orthopedic implants: a literature review, Biomed. Mater. 15 (2020), 052003, https://doi.org/10.1088/1748-605X/ab9078.
[50] M. Bollman, R. Malbrue, C. Li, H. Yao, S. Guo, S. Yao, Improvement of osseointegration by recruiting stem cells to titanium implants fabricated with 3D printing, Ann. N. Y. Acad. Sci. 1463 (2020) 37–44, https://doi.org/10.1111/nyas.14251.
[51] G. Heart, Protection Study Collaborative, Effects on 11-year mortality and morbidity of lowering LDL cholesterol with simvastatin for about 5 years in 20,536 high-risk individuals: a randomised controlled trial, Lancet 378 (2011) 2013–2020, https://doi.org/10.1016/S0140-6736(11)61125-2.
[52] V. Kansal, A.J. Burnham, B.L.C. Kinney, N.F. Saba, C. Paulos, G.B. Lesinski, Z. S. Buchwald, N.C. Schmitt, Statin drugs enhance responses to immune checkpoint blockade in head and neck cancer models, J. Immunother. Cancer. 11 (2023), https://doi.org/10.1136/jitc-2022-005940.
[53] F. Iannelli, M.S. Roca, R. Lombardi, C. Ciardiello, L. Grumetti, S. De Rienzo, T. Moccia, C. Vitagliano, A. Sorice, S. Costantini, M.R. Milone, B. Pucci, A. Leone, E. Di Gennaro, R. Mancini, G. Ciliberto, F. Bruzzese, A. Budillon, Synergistic antitumor interaction of valproic acid and simvastatin sensitizes prostate cancer to docetaxel by targeting CSCS compartment via YAP inhibition, J. Exp. Clin. Cancer Res. 39 (2020) 213, https://doi.org/10.1186/s13046-020-01723-7.
[54] W. Yuan, B. Hai, X. Ren, J. Zhu, C. Zhang, Z. Guan, J. Jia, H. Wang, B. Cao, C. Song, Single-dose local intraosseous injection of simvastatin suppresses breast cancer with tumor vascular normalization, Transl. Oncol. 13 (2020), 100867, https://doi.org/10.1016/j.tranon.2020.100867.
[55] Y. Li, G. Toraldo, A.M. Li, X.Y. Yang, H.Y. Zhang, W.P. Qian, M.N. Weitzmann, B cells and T cells are critical for the preservation of bone homeostasis and attainment of peak bone mass in vivo, Blood 109 (2007) 3839–3848, https://doi.org/10.1182/blood-2006-07-037994.
[56] K.K. Patel, V.S. Sehgal, K. Kashfi, Molecular targets of statins and their potential side effects: not all the glitter is gold, Eur. J. Pharmacol. 922 (2022), 174906, https://doi.org/10.1016/j.ejphar.2022.174906.

[57] M.H. Gao, P. Monian, N. Quadri, R. Ramasamy, X.J. Jiang, Glutaminolysis and transferrin regulate ferroptosis, Mol. Cell. 59 (2015) 298–308, https://doi.org/10.1016/j.molcel.2015.06.011.
[58] Y.C. Xie, S. Zhu, X.X. Song, X.F. Sun, Y. Fan, J.B. Liu, M. Zhong, H. Yuan, L. Zhang, T.R. Billiar, M.T. Lotze, H.J. Zeh, R. Kang, G. Kroemer, D.L. Tang, The tumor suppressor p53 limits ferroptosis by blocking DPP4 activity, Cell Rep. 20 (2017) 1692–1704, https://doi.org/10.1016/j.celrep.2017.07.055.
[59] W.H. Yang, Z.Q. Huang, J.L. Wu, C.C. Ding, S.K. Murphy, J.T. Chi, A TAZ-ANGPTL4-NOX2 axis regulates ferroptotic cell death and chemoresistance in epithelial ovarian cancer, Mol. Cancer Res. 18 (2020) 79–90, https://doi.org/10.1158/1541-7786.MCR-19-0691.
[60] I. Poursaitidis, X. Wang, T. Crighton, C. Labuschagne, D. Mason, S.L. Cramer, K. Triplett, R. Roy, O.E. Pardo, M.J. Seckl, S.W. Rowlinson, E. Stone, R.F. Lamb, Oncogene-selective sensitivity to synchronous cell death following modulation of the amino acid nutrient cystine, Cell Rep. 18 (2017) 2547–2556, https://doi.org/10.1016/j.celrep.2017.02.054.
[61] X.Q. Chen, S.D. Xu, C.X. Zhao, B. Liu, Role of TLR4/NADPH oxidase 4 pathway in promoting cell death through autophagy and ferroptosis during heart failure, Biochem. Biophys. Res. Commun. 516 (2019) 37–43, https://doi.org/10.1016/j.bbrc.2019.06.015.
[62] W.H. Yang, C.C. Ding, T.A. Sun, G. Rupprecht, C.C. Lin, D. Hsu, J.T. Chi, The hippo pathway effector TAZ regulates ferroptosis in renal cell carcinoma, Cell Rep. 28 (2019) 2501–2508, https://doi.org/10.1016/j.celrep.2019.07.107, e4.
[63] X. Yao, R. Xie, Y. Cao, J. Tang, Y. Men, H. Peng, W. Yang, Simvastatin induced ferroptosis for triple-negative breast cancer therapy, J. Nanobiotechnol. 19 (2021) 311, https://doi.org/10.1186/s12951-021-01058-1.
[64] D. Zhou, Q. Wu, H. Qiu, M. Li, Y. Ji, Simvastatin inhibits endometrial cancer malignant behaviors by suppressing RAS/mitogen-activated protein kinase (MAPK) pathway-mediated reactive oxygen species (ROS) and ferroptosis, Evid. Based Complement, Alternative Med. 2022 (2022), 6177477, https://doi.org/10.1155/2022/6177477.
[65] Y.E. Elakkad, S.N.S. Mohamed, N.Z. Abuelezz, Potentiating the Cytotoxic Activity of a Novel Simvastatin-Loaded Cubosome against Breast Cancer Cells: Insights on Dual Cell Death via Ferroptosis and Apoptosis, Breast Cancer, vol. 13, dove Med press, 2021, pp. 675–689, https://doi.org/10.2147/BCTT.S336712.
[66] G. Mundy, R. Garrett, S. Harris, J. Chan, D. Chen, G. Rossini, B. Boyce, M. Zhao, G. Gutierrez, Stimulation of bone formation in vitro and in rodents by statins, Science 286 (1999) 1946–1949, https://doi.org/10.1126/science.286.5446.1946.
[67] G. Vogel, Cholesterol-lowering drugs may boost bones, Science 286 (1999) 1825–1826, https://doi.org/10.1126/science.286.5446.1825a.
[68] S. Tao, S.Q. Chen, W.T. Zhou, F.Y. Yu, L. Bao, G.X. Qiu, Q. Qiao, F.Q. Hu, J. W. Wang, H. Yuan, A novel biocompatible, simvastatin-loaded, bone-targeting lipid nanocarrier for treating osteoporosis more effectively, RSC Adv. 10 (2020) 20445–20459, https://doi.org/10.1039/d0ra00685h.